Plasma Physics and
Controlled Fusion



**PAPER • OPEN ACCESS**

# Effect of triangularity on plasma turbulence and the SOL-width scaling in L-mode diverted tokamak configurations

To cite this article: K Lim *et al* 2023 *Plasma Phys. Control. Fusion* **65** 085006

OPEN ACCESS
IOP Publishing
Plasma Physics and Controlled Fusion
Plasma Phys. Control. Fusion **65** (2023) 085006 (17pp)
https://doi.org/10.1088/1361-6587/acdc52

# Effect of triangularity on plasma turbulence and the SOL-width scaling in L-mode diverted tokamak configurations

**K Lim[1,*], M Giacomin[2], P Ricci[1], A Coelho[1], O Février[1], D Mancini[1], D Silvagni[3] and L Stenger[1]**

[1] Ecole Polytechnique Fédérale de Lausanne (EPFL), Swiss Plasma Center, EPFL SB SPC, Station 13, CH-1015 Lausanne, Switzerland
[2] York Plasma Institute, University of York, YO10 5DD York, United Kingdom
[3] Max-Planck-Institut für Plasmaphysik, Boltzmannstr. 2, D-85748 Garching, Germany

E-mail: kyungtak.lim@epfl.ch

Received 4 March 2023, revised 17 May 2023
Accepted for publication 7 June 2023
Published 20 June 2023

**Abstract**

The effect of triangularity on tokamak boundary plasma turbulence is investigated using global, flux-driven, three-dimensional, two-fluid simulations. The simulations show that negative triangularity (NT) stabilizes boundary plasma turbulence, and linear investigations reveal that this is due to a reduction of the magnetic curvature driven by interchange instabilities, such as the resistive ballooning mode (RBM). As a consequence, the pressure decay length $L_p$, related to the scrape-off layer (SOL) power fall-off length $\lambda_q$, is found to be affected by triangularity. Leveraging considerations on the effect of triangularity on the linear growth rate and nonlinear evolution of the RBM, the analytical theory-based scaling law for $L_p$ in L-mode plasmas, derived by Giacomin *et al* (2021 *Nucl. Fusion* **61** 076002), is extended to include the effect of triangularity. The scaling is in agreement with nonlinear simulations and a multi-machine experimental database, which includes recent TCV discharges dedicated to the study of the effect of triangularity in L-mode diverted discharges. Overall, the present results highlight that NT narrows the $L_p$ and considering the effect of triangularity is important for a reliable extrapolation of $\lambda_q$ from present experiments to larger devices.

Keywords: negative triangularity, edge plasma turbulence, SOL width scaling

(Some figures may appear in colour only in the online journal)

## 1. Introduction

The shape of the plasma cross-section plays an important role in determining the performance of a tokamak. An elongated D-shape plasma was introduced in JET based on its improved magnetohydrodynamics (MHD) stability properties [1, 2] and enhanced confinement time obtained by operating in H-mode conditions [3]. In H-mode plasmas, however, the formation of a steep pressure gradient in the edge region, also known as *pedestal*, often yields transient edge-localized modes (ELMs) that release a large amount of energy (∼MJ) across the separatrix [4]. ELMs can severely damage wall components and overcome the material limits, constraining the operational space of future devices [5].

Recently, the negative triangularity (NT) scenario has attracted increasing attention as an alternative to the H-mode operation in positive triangularity (PT) [6]. The first detailed

[*] Author to whom any correspondence should be addressed.

study focused on the dependence of the confinement time on triangularity, $\delta$, was carried out in TCV with auxiliary electron cyclotron heating in L-mode operation [7, 8]. The scaling law for energy confinement, found to obey $\tau_E \propto (1+\delta)^{-0.35}$, indicates the increase in energy confinement time in NT plasma, $\delta < 0$, with respect to PT scenario, $\delta > 0$. Following this initial investigation, a large number of experimental studies on NT were carried out on the TCV [9–13], DIII-D [14–16] and ASDEX Upgrade (AUG) [17] tokamaks, showing H-mode like confinement ($H_{98y2} = 1.3$) and ITER-relevant beta ($\beta_N = 2.7$) in an intrinsically ELM-free L-mode regime. The effects of plasma shaping on confinement time were actively investigated also through first-principle numerical codes. Both gyrokinetic and gyrofluid simulations [18–22] shed light on the stabilizing effect of NT over both the ion temperature gradient (ITG) mode and the trapped electron mode (TEM).

Turning to the boundary, recent works with fluid models [23, 24] provide insight on edge plasma turbulence in NT plasma, showing a reduction of the power fall-off length $\lambda_q$ for $\delta < 0$. The observed reduction in the scrape-off layer (SOL) width [25] is interpreted as the result of the suppression of plasma turbulence, but recent experimental work also shows that the plasma interactions with the first wall might contribute to a narrower $\lambda_q$ in NT than in PT configurations [26]. As a matter of fact, the reduced $\lambda_q$ in the SOL, which might be a drawback for the use of NT configurations in future fusion reactors, calls for a careful analysis of plasma turbulence in NT scenarios.

The purpose of this paper is to explore the effect of triangularity on edge plasma turbulence and, as a consequence, on the scaling law of the power fall-off length $\lambda_q$. The present work leverages previous simulations [23, 27], carried out with the global Braginskii Solver (GBS) code, which reveal the stabilizing effect of NT on SOL plasma turbulence in a limited configuration. In the present paper, we extend these investigations to consider a diverted configuration, taking into account the interplay existing between the core, edge and SOL regions. We first discuss the results of global, flux-driven, nonlinear, three-dimensional, two-fluid GBS simulations in PT and NT magnetic geometries, particularly in view of the stabilizing effects of NT on edge plasma turbulence. Second, we analyze the effect of plasma shaping on turbulence, deriving a theoretical scaling law for the pressure gradient length $L_p$ that extends the work presented in [28, 29] to include the effect of plasma triangularity. Finally, the derived scaling law is compared with nonlinear simulations and a multi-machine experimental database that includes recent discharges carried out on the TCV tokamak to study the effect of triangularity on plasma turbulence, as well as discharges from the AUG [30], Alcator C-Mod [31], COMPASS [32], JET [33] and MAST [34] tokamaks for L-mode plasmas.

We focus on the sheath-limited regime, characterized by a small temperature gradient between the upstream (i.e. outboard midplane) and the divertor targets, in contrast to the conduction-limited regime [35]. The two regimes can be identified by using the SOL collisionality parameter $\nu^* = 10^{-16} n_u L / T_u^2$ derived from the two-point model [35], where $u$ denotes the upstream quantities, $L$ is the connection length and $n, T$ and $L$ are expressed in $\mathrm{m}^{-3}$, eV and m, respectively. In general, the sheath-limited regime is characterized by weak collisionality ($\nu^* < 10$) while a significant temperature drop is often observed in the conduction-limited regime ($\nu^* > 15$).

The remainder of this paper is organized as follows. In section 2, we introduce the physical model to study boundary plasma turbulence. The results of nonlinear GBS simulations are then discussed in section 3 focusing on the stabilizing effect of NT on edge plasma turbulence. The theoretical derivation of the scaling law of the pressure decay length, $L_p$, which takes into account plasma shaping parameters, is detailed in section 4 and comparisons with nonlinear simulation results are presented. In section 5, the validity of our newly derived scaling law is tested against a multi-machine experimental database. Finally, the conclusions are drawn in section 6.

## 2. Numerical model

The high plasma collisionality ($L_\parallel \gg \lambda_e$, $L_\parallel$ being the parallel length scales of turbulent modes and $\lambda_e$ the electron mean-free path) justifies the use of the two-fluid Braginskii model to study boundary plasma turbulence in L-mode discharges. In addition, the drift limit of the Braginskii model [36] can be considered since plasma turbulence in the boundary region occurs on time scales slower than $1/\Omega_{ci}$, being $\Omega_{ci} = eB/m_i$ the ion cyclotron frequency.

Initially developed to study turbulence in basic plasma physics experiments [37] and limited tokamak configurations, the GBS code [38–40] solves the drift-reduced Braginskii equations to evolve plasma turbulence at the tokamak boundary. The implementation of a spatial discretization algorithm independent of the magnetic field [41] allows GBS to simulate diverted configurations with an arbitrary magnetic equilibrium [42, 43], as well as non-axisymmetric configurations, such as the stellarators [44]. While the plasma model implemented in GBS was developed in recent years to include the neutral dynamics [45], we do not include it in the simulations presented here, therefore focusing on the sheath-limited regime, where only pure plasma composed of ions and electrons, without radiative impurities, is considered in the present study. We also neglect electromagnetic effects that can be important at high values of plasma beta [46]. Accordingly, the GBS equations considered in the present study can be written in dimensionless form as:

$$\frac{\partial n}{\partial t} = -\frac{\rho_*^{-1}}{B}[\phi, n] + \frac{2}{B}\left[C(p_e) - nC(\phi)\right] - \nabla_\parallel (n v_{\parallel e}) + D_n \nabla_\perp^2 n + s_n, \tag{2.1}$$

$$\frac{\partial \Omega}{\partial t} = -\frac{\rho_*^{-1}}{B}\nabla\cdot[\phi, \omega] - \nabla\cdot\left(v_{\parallel i}\nabla_\parallel \omega\right) + B^2 \nabla_\parallel j_\parallel + 2BC(p_e + \tau p_i) + \frac{B}{3}C(G_i) + D_\Omega \nabla_\perp^2 \Omega, \tag{2.2}$$

$$\frac{\partial v_{\|i}}{\partial t} = -\frac{\rho_*^{-1}}{B}[\phi, v_{\|i}] - v_{\|i}\nabla_\| v_{\|i} - \frac{1}{n}\nabla_\|(p_e + \tau p_i) - \frac{2}{3n}\nabla_\| G_i + D_{v_{\|i}}\nabla_\perp^2 v_{\|i}, \tag{2.3}$$

$$\frac{\partial v_{\|e}}{\partial t} = -\frac{\rho_*^{-1}}{B}[\phi, v_{\|,e}] - v_{\|e}\nabla_\| v_{\|e} + \frac{m_i}{m_e}\left(\nu j_\| + \nabla_\|\phi - \frac{1}{n}\nabla_\| p_e - 0.71\nabla_\| T_e - \frac{2}{3n}\nabla_\| G_e\right) + D_{v_{\|e}}\nabla_\perp^2 v_{\|e}, \tag{2.4}$$

$$\frac{\partial T_i}{\partial t} = -\frac{\rho_*^{-1}}{B}[\phi, T_i] - v_{\|i}\nabla_\| T_i + \frac{4}{3}\frac{T_i}{B}\left[C(T_e) + \frac{T_e}{n}C(n) - C(\phi)\right] - \frac{10}{3}\tau\frac{T_i}{B}C(T_i) + \frac{2}{3}T_i\left[(v_{\|i} - v_{\|e})\frac{\nabla_\| n}{n} - T_i\nabla_\| v_{\|e}\right] + 2.61\nu n(T_e - \tau T_i) + \nabla_\|(\chi_{\|i}\nabla_\| T_i) + D_{T_i}\nabla_\perp^2 T_i + s_{T_i}, \tag{2.5}$$

$$\frac{\partial T_e}{\partial t} = -\frac{\rho_*^{-1}}{B}[\phi, T_e] - v_{\|e}\nabla_\| T_e + \frac{2}{3}T_e\left[0.71\frac{\nabla_\| j_\|}{n} - \nabla_\| v_{\|e}\right] - 2.61\nu n(T_e - \tau T_i) + \frac{4}{3}\frac{T_e}{B}\left[\frac{7}{2}C(T_e) + \frac{T_e}{n}C(n) - C(\phi)\right] + \nabla_\|(\chi_{\|e}\nabla_\| T_e) + D_{T_e}\nabla_\perp^2 T_e + s_{T_e}. \tag{2.6}$$

Equations (2.1)–(2.6) are closed by the evaluation of the electrostatic potential that avoids the Boussinesq approximation,

$$\nabla\cdot(n\nabla_\perp\phi) = \Omega - \tau\nabla_\perp^2 p_i, \tag{2.7}$$

where $\Omega = \nabla\cdot\omega = \nabla\cdot(n\nabla_\perp\phi + \tau\nabla_\perp p_i)$ is the scalar vorticity.

In equations (2.1)–(2.6) and in the remainder of this paper, the plasma density $n$, the ion and electron temperatures, $T_i$ and $T_e$, the ion and electron parallel velocities, $v_{\|i}$ and $v_{\|e}$, and the electrostatic potential $\phi$ are normalized to the reference values $n_0, T_{i0}, T_{e0}, c_{s0} = \sqrt{T_{e0}/m_i}, c_{s0}$, and $T_{e0}/e$, respectively. The perpendicular lengths are normalized to the ion sound Larmor radius, $\rho_{s0} = c_{s0}/\Omega_{ci}$, and parallel lengths are normalized to the tokamak major radius, $R_0$. Time is normalized to $t_0 = R/c_{s0}$. In addition, the dimensionless parameters that determine the plasma dynamics in equations (2.1)–(2.7) are the normalized ion sound Larmor radius, $\rho_* = \rho_{s0}/R_0$, the ratio of the ion to the electron temperature, $\tau = T_{i0}/T_{e0}$, the normalized ion and electron viscosities, $\eta_{0,i}$ and $\eta_{0,e}$, the normalized ion and electron parallel thermal conductivities $\chi_{\|i}$ and $\chi_{\|e}$, and the normalized Spitzer resistivity $\nu = e^2 n_0 R_0/(m_i c_{s0}\sigma_\|) = \nu_0 T_e^{-3/2}$, with

$$\sigma_\| = \left(1.96\frac{n_0 e^2\tau_e}{m_e}\right)n = \left[\frac{5.88}{4\sqrt{2\pi}}\frac{(4\pi\epsilon_0)^2}{e^2}\frac{T_{e0}^{3/2}}{\lambda\sqrt{m_e}}\right]T_e^{3/2} \tag{2.8}$$

and, as a consequence,

$$\nu_0 = \frac{4\sqrt{2\pi}}{5.88}\frac{e^4}{(4\pi\epsilon_0)^2}\frac{\sqrt{m_e}R_0 n_0\lambda}{m_i c_{s0}T_{e0}^{3/2}}, \tag{2.9}$$

where $\lambda$ is the Coulomb logarithm. The gyroviscous terms are defined as

$$G_i = -\eta_{0i}\left[2\nabla_\| v_{\|i} + \frac{1}{B}C(\phi) + \frac{1}{enB}C(p_i)\right] \tag{2.10}$$

and

$$G_e = -\eta_{0e}\left[2\nabla_\| v_{\|e} + \frac{1}{B}C(\phi) - \frac{1}{enB}C(p_e)\right], \tag{2.11}$$

where $\eta_{0i} = 0.96nT_i\tau_i$ and $\eta_{0e} = 0.73nT_e\tau_e$. The diffusion terms $D_f\nabla_\perp^2 f$ are added on the right hand side of equations (2.1)–(2.6) to improve the numerical stability of the simulations.

The GBS numerical grid employs a uniform Cartesian grid that discretizes the radial, vertical, and toroidal directions (i.e. the $R, Z$, and $\varphi$ coordinates). The number of grid points is $N_R\times N_Z\times N_\varphi$. The grid spacing, indicated as $\Delta R$, $\Delta Z$ and $\Delta\varphi$, is constant across the entire domain. Details on the numerical grid are reported in [40].

The spatial operators that appear in equations (2.1)–(2.7) are the Poisson bracket operator, $[f,g] = \boldsymbol{b}\cdot(\nabla g\times\nabla f)$, the curvature operator, $C(f) = B[\nabla\times(\boldsymbol{b}/B)]/2\cdot\nabla f$, the parallel gradient operator, $\nabla_\| f = \boldsymbol{b}\cdot\nabla f$, and the perpendicular Laplacian operator, $\nabla_\perp^2 f = \nabla\cdot[(\boldsymbol{b}\times\nabla f)\times\boldsymbol{b}]$, where $\boldsymbol{b} = \boldsymbol{B}/B$ is the unit vector of the magnetic field. It is useful to represent these operators in tensorial form for an arbitrary magnetic field [47],

$$[\phi, f] = \frac{1}{\mathcal{J}}\epsilon_{ijk}b_i\frac{\partial\phi}{\partial\xi^j}\frac{\partial f}{\partial\xi^k}, \tag{2.12}$$

$$\nabla_\| f = b^j\frac{\partial f}{\partial\xi^j}, \tag{2.13}$$

$$C(f) = \frac{B}{2\mathcal{J}}\frac{\partial c_m}{\partial\xi^j}\frac{\partial f}{\xi^k}\epsilon_{kjm}, \tag{2.14}$$

$$\nabla_\perp^2 f = \frac{1}{\mathcal{J}}\frac{\partial}{\partial\xi^k}\left(\mathcal{J}^{-1}\epsilon_{klm}\epsilon_{i\alpha\beta}g_{mi}b_l b_\alpha\frac{\partial f}{\partial\xi^\beta}\right), \tag{2.15}$$

where the Einstein convention is used with the Levi-Civita symbol $\varepsilon_{ijk}$, and we introduce an arbitrary set of coordinates $\boldsymbol{\xi} = (\xi^1, \xi^2, \xi^3)$, the coefficients $c_m = b_m/B$, and $b_i = g_{ij}b^j$, the covariant metric tensor $g^{ij} = \nabla\xi^i\cdot\nabla\xi^j$ and the Jacobian $\mathcal{J} = 1/\sqrt{\det(g^{ij})}$. In addition, we express $\nabla\cdot\boldsymbol{b} = \frac{1}{\mathcal{J}}\frac{\partial}{\partial\xi^i}(b^i\mathcal{J})$.

The axisymmetric magnetic field in GBS is represented as $\boldsymbol{B} = RB_\varphi\nabla\varphi + \nabla\varphi\times\nabla\psi$ where the poloidal flux function $\psi$ and the toroidal angle $\varphi$ are introduced. The non-field-aligned cylindrical coordinates $(R,\varphi,Z)$ is used, where $R$ corresponds to the radial distance from the tokamak symmetry axis and $Z$ is the vertical coordinate. By considering the large aspect ratio limit ($\epsilon \ll 1$), assuming $\delta \sim B_p/B_\varphi \ll 1$, and retaining only the leading order terms in $\varepsilon$ and $\delta$, the differential operators in equations (2.12)–(2.15) implemented in GBS can be recast as

$$[\phi,f] = \frac{B_\varphi}{B}(\partial_Z\phi\,\partial_R f - \partial_R\phi\,\partial_Z f), \tag{2.16}$$

$$\nabla_\| f = \partial_Z\psi\,\partial_R f - \partial_R\psi\,\partial_Z f + \frac{B_\varphi}{B}\partial_\varphi f, \tag{2.17}$$

$$\mathcal{C}(f) = \frac{B_\varphi}{B}\partial_Z f, \tag{2.18}$$

$$\nabla_\perp^2 f = \partial_{RR}^2 f + \partial_{ZZ}^2 f. \tag{2.19}$$

The presence of the density source in the proximity of the last closed flux surface (LCFS) mimics the ionization of neutral atoms and the temperature source the Ohmic heating in the core. The analytical expressions of source terms are expressed as

$$s_n = s_{n0}\exp\left\{-\frac{[\psi(R,Z)-\psi_n]^2}{\Delta_n^2}\right\} \tag{2.20}$$

and

$$s_T = \frac{s_{T0}}{2}\left[\tanh\left[-\frac{\psi(R,Z)-\psi_T}{\Delta_T}\right]+1\right], \tag{2.21}$$

where $\psi_n$ and $\psi_T$ represent two flux surfaces located inside the LCFS, while $\Delta_n$ and $\Delta_T$ determine the radial width of the source terms.

The boundary conditions imposed on the magnetic presheath, where the ion drift approximation is not valid, are derived in [48] to generalize the Bohm–Chodura criterion, and are adapted to the diverted configuration [41]. By neglecting the terms associated with the plasma gradients along the wall, these boundary conditions for the top and bottom walls can be expressed as

$$v_{\|i} = \pm\sqrt{T_e+\tau T_i}, \tag{2.22}$$

$$v_{\|e} = \pm\sqrt{T_e+\tau T_i}\max\left[\exp\left(\Lambda-\frac{\phi}{T_e}\right),\exp(\Lambda)\right], \tag{2.23}$$

$$\partial_Z n = \mp\frac{n}{\sqrt{T_e+\tau T_i}}\partial_Z v_{\|i}, \tag{2.24}$$

$$\partial_Z\phi = \mp\frac{T_e}{\sqrt{T_e+\tau T_i}}\partial_Z v_{\|i}, \tag{2.25}$$

$$\partial_Z T_e = \partial_Z T_i = 0, \tag{2.26}$$

$$\Omega = \mp n\sqrt{T_e+\tau T_i}\partial_Z^2 v_{\|i}, \tag{2.27}$$

where the $\pm$ sign indicates the magnetic field lines entering (top sign) or leaving (bottom sign) the wall and $\Lambda \simeq 3$. Moreover, the electric potential is chosen to be $\phi = \Lambda T_e$ at the left and right walls of the simulation domain, and vanishing perpendicular derivatives to the wall are set for the other quantities. Flat density and temperature profiles with small random noise of amplitude $10^{-6}$ are used as initial conditions, while the initial profiles of $v_{\|e}$ and $v_{\|i}$ are chosen to satisfy the boundary conditions. The system is evolved until it reaches a quasi-steady state that is expected to be independent of the initial conditions [28].

In order to analyze the simulation results, we make use of a linear solver based on a local flux-tube coordinate system. This system of coordinates is based on the toric coordinate system ($\Psi = r, \Theta = a\theta_*, \zeta = R_0\varphi$) where $a$ is the minor radius and the straight-field-line angle $\theta_*$ is defined as

$$\theta_* = \frac{1}{q(r)}\int_0^\theta \frac{\boldsymbol{B}\cdot\nabla\varphi}{\boldsymbol{B}\cdot\nabla\theta'}d\theta', \tag{2.28}$$

being $\theta$ and $\theta'$ the poloidal angle, and $q(r)$ the safety factor

$$q(r) = \frac{1}{2\pi}\int_0^{2\pi}\frac{\boldsymbol{B}\cdot\nabla\varphi}{\boldsymbol{B}\cdot\nabla\theta}d\theta. \tag{2.29}$$

This field-aligned system is then transformed into the flux-tube coordinates $(r,\alpha,\theta_*)$ where $\alpha = \varphi - q(r)\theta_*$ is a field line label, and finally rescaled into the local flux-tube coordinates as $x = r, y = (a/q)\alpha, z = qR_0\theta_*$. The $(x,y)$ plane is perpendicular to the magnetic field, and $z$ is a field-aligned coordinate. In the rescaled flux-tube coordinate system, the geometrical operators in equations (2.12)–(2.15) can be rewritten as

$$[\phi,f] = \mathcal{P}_{xy}[\phi,f]_{xy} + \mathcal{P}_{yz}[\phi,f]_{yz} + \mathcal{P}_{zx}[\phi,f]_{zx}, \tag{2.30}$$

$$\nabla_\| f = \mathcal{D}^x\frac{\partial f}{\partial x} + \mathcal{D}^y\frac{\partial f}{\partial y} + \mathcal{D}^z\frac{\partial f}{\partial z}, \tag{2.31}$$

$$\mathcal{C}(f) = \mathcal{C}^x\frac{\partial f}{\partial x} + \mathcal{C}^y\frac{\partial f}{\partial y} + \mathcal{C}^z\frac{\partial f}{\partial z}, \tag{2.32}$$

$$\nabla_\perp^2 f = \mathcal{N}^x\frac{\partial f}{\partial x} + \mathcal{N}^y\frac{\partial f}{\partial y} + \mathcal{N}^z\frac{\partial f}{\partial z} + \mathcal{N}^{xx}\frac{\partial^2 f}{\partial x^2} + \mathcal{N}^{xy}\frac{\partial^2 f}{\partial x\partial y} \tag{2.33}$$

$$+\mathcal{N}^{yy}\frac{\partial^2 f}{\partial y^2} + \mathcal{N}^{xz}\frac{\partial^2 f}{\partial x\partial z} + \mathcal{N}^{yz}\frac{\partial^2 f}{\partial y\partial z} + \mathcal{N}^{zz}\frac{\partial f}{\partial z^2}, \tag{2.34}$$

where the coefficients appearing in front of the spatial derivatives are computed as a function of plasma shaping parameters. Detailed expressions for these coefficients are derived in appendix A.

## 3. Nonlinear analysis

We describe a set of nonlinear GBS simulations used to investigate the effect of triangularity on boundary plasma turbulence. All simulations presented herein use a numerical grid $N_R \times N_Z \times N_\varphi = 240 \times 320 \times 80$ and a time step $\Delta t = 10^{-5} \times R_0/c_{s0}$. The size of the simulation domain is set to $L_R = 600\rho_{s0}, L_Z = 800\rho_{s0}$ and $\rho_* = \rho_{s0}/R_0 = 1/700$. As a reference, we note that, considering $B_T = 0.9\,\mathrm{T}$ and $T_{e0} = 20\,\mathrm{eV}$, the normalizing parameters are $c_{s0} = 3.8 \times 10^4\,\mathrm{m\,s^{-1}}$, $\rho_{s0} = 0.5\,\mathrm{mm}$. They yield $L_R \simeq 30\,\mathrm{cm}, L_Z \simeq 40\,\mathrm{cm}$ and $R_0 \simeq 25\,\mathrm{cm}$, corresponding to a tokamak with 1/3 of the TCV size [49], approximately. We note that the computation time required by a GBS simulation increases significantly with the system size. Therefore, in order to explore various collisionality values in NT and PT plasmas, we restrict ourselves to simulations with relatively small system size. Other plasma parameters are kept constant throughout the present study, such as $\tau = T_{i0}/T_{e0} = 1$, $m_i/m_e = 200$, $\eta_{0e} = \eta_{0i} = 1$ and $\chi_{\parallel e} = \chi_{\parallel i} = 1$. The use of a small ratio $m_i/m_e = 200$ reduces the computational cost of our simulations, and it is not expected to significantly affect our simulations results because resistive effects dominate over inertial effects when $\nu > (m_e/m_i)\gamma$, which is the case for our simulations. The direction of the toroidal magnetic field $B_T$ is set for the ion-$\nabla B$ drift being away from the X-point (*unfavorable* direction for H-mode access). In addition, we use $a/R_0 = 0.3$ and the plasma current on the axis is chosen to have a safety factor $q_0 \simeq 1$ at the magnetic axis and $q_{95} \simeq 4$ at the tokamak edge.

The magnetic geometries of the NT and PT plasmas that we consider in the present study are shown in figure 1. These equilibria are constructed by solving the Biot–Savart law in the infinite aspect-ratio limit with a Gaussian-like centered current and additional current filaments outside the simulation domain. The magnetic equilibria shown in figure 1 are characterized by an elongation $\kappa \simeq 1.3$ and triangularity $\delta \simeq \pm 0.3$. Denoting $Z_{\max}, R_{\max}$ and $Z_{\min}, R_{\min}$ as the maximum and minimum values of $Z$ and $R$ along the separatrix, the shaping parameters are defined as [50]

$$\kappa = \frac{Z_{\max} - Z_{\min}}{R_{\max} - R_{\min}}, \tag{3.1}$$

and

$$\delta = \frac{\delta_{\text{upper}} + \delta_{\text{lower}}}{2}, \tag{3.2}$$

where $\delta_{\text{upper}}$ and $\delta_{\text{lower}}$ denote the upper and lower triangularity, respectively, being

$$\delta_{\text{upper}} = \frac{R_0 - R(Z = Z_{\max})}{a} \tag{3.3}$$

and

$$\delta_{\text{lower}} = \frac{R_0 - R(Z = Z_{\min})}{a}, \tag{3.4}$$

with

$$R_0 = \frac{R_{\max} + R_{\min}}{2} \tag{3.5}$$

and

$$a = \frac{R_{\max} - R_{\min}}{2}. \tag{3.6}$$

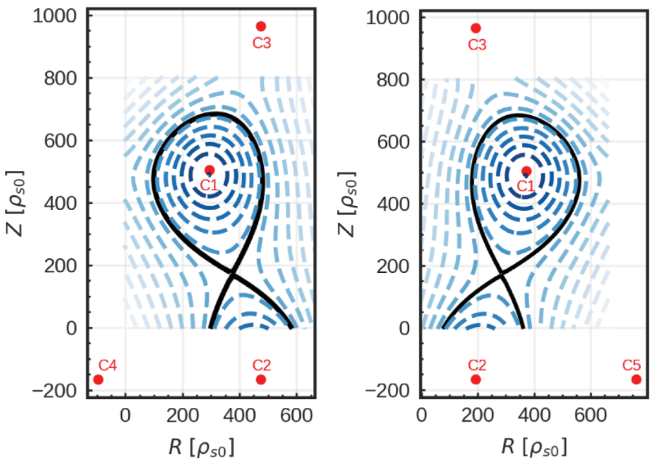

(a) Negative triangularity (b) Positive triangularity

**Figure 1.** Magnetic equilibrium profiles are used for the nonlinear GBS simulations of NT ($\delta \simeq -0.3$) and PT ($\delta \simeq +0.3$) plasmas with $\kappa \simeq 1.3$. The red dots represent the position of the current that generates the magnetic field, i.e. the main plasma current (C1), the divertor current (C2), the upper shaping current (C3), the left shaping current (C4) and the right shaping current (C5).

Recent study carried out on TCV report that decreasing $\delta_{\text{upper}}$ reduces the amplitude of turbulent fluctuations and leads to an increased confinement time, while $\delta_{\text{lower}}$ affects mostly the plasma turbulence in the boundary near the X-point by modifying the divertor geometry [25]. In the present study, the sign of both $\delta_{\text{lower}}$ and $\delta_{\text{upper}}$ is reversed when obtaining $\delta = \pm 0.3$.

Different turbulent regimes in the tokamak boundary are observed in GBS, depending on the edge collisionality and input heat power [28], as they result from different driving instabilities, such as the resistive ballooning modes (RBMs) and resistive drift waves (RDWs) [36, 51]. The plasma collisionality and heating source in our simulations are chosen so that our simulations are in the RBM regime, which is equivalent to the L-mode operational regime of tokamaks. In particular, being destabilized mainly by the magnetic field curvature and plasma pressure gradient, RBMs are known to be strongly affected by the plasma shaping, while their impact is less important on RDWs [23].

The simulations described in this paper are analyzed in the quasi-steady state regime established when plasma sources, perpendicular transport and losses to the vessel wall balance each other and all quantities fluctuate around constant values. Once the simulations reach this quasi-steady state, all quantities are toroidally averaged over a $10t_0$ time frame to evaluate the equilibrium profiles. In the present paper, fluctuating quantities are expressed in terms of tilde and time- and toroidally-averaged quantities with an overline, e.g. $\phi = \bar{\phi} + \tilde{\phi}$.

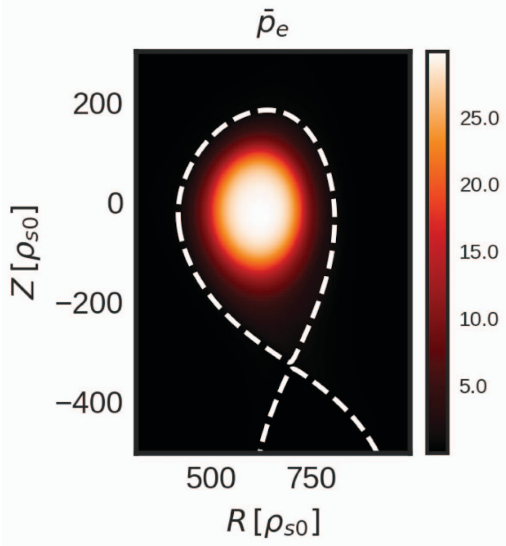


(a) NT ($\delta = -0.3$) plasma

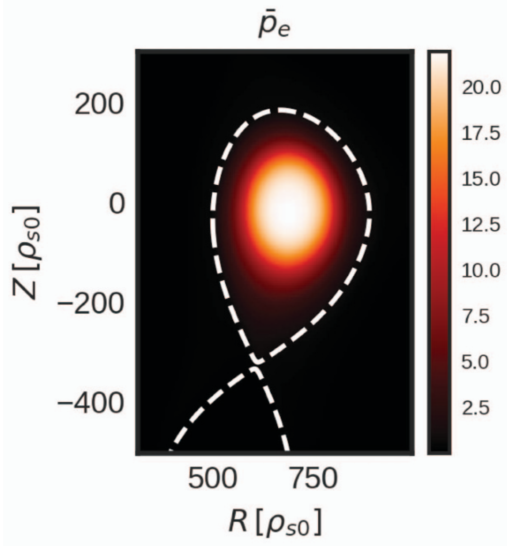


(b) PT ($\delta = +0.3$) plasma

**Figure 2.** The poloidal cross section of the equilibrium electron pressure for NT and PT plasmas with $s_{T0} = 0.025$ and $\nu_0 = 0.1$. The dashed white line represents the separatrix.

Figure 2 displays the equilibrium electron pressure, $\bar{p}_e$, in PT and NT simulations revealing higher plasma pressure in the case of the NT plasma, despite the same sources ($s_{T0} = s_{n0} = 0.075$) being used in the two simulations. Higher $\bar{p}_e$ values are associated with a reduced transport level and a higher confinement time. The qualitative estimate of the electron energy confinement time $\tau_E$ is evaluated from the plasma energy content inside LCFS divided by heating power,

$$\tau_E = \frac{3}{2}\frac{\int_{A_{\mathrm{LCFS}}} \bar{p}_e dRdZ}{\int_{A_{\mathrm{LCFS}}} s_p dRdZ}, \tag{3.7}$$

and it is shown for different values of edge collisionality in figure 3. The analysis reveals an improved energy confinement time for $\delta < 0$, in agreement with experimental observations from TCV [9, 10, 13] and DIII-D [14, 15]. The energy confinement time for both NT and PT decreases as the collisionality increases. In fact, transport driven by RBMs increases with collisionality leading to reduced energy confinement time for the same value of the input power.

In agreement with these observations, first-principle simulations based on a gyrokinetic model [15, 20] show that NT plasmas are characterized by density and temperature fluctuations of reduced amplitude, yielding an enhanced confinement time. However, the reason for the higher confinement is attributed to kinetic effects that stabilize linear instabilities, such as the TEMs and the ITG modes. Kinetic effects are not retained in our fluid simulations, affecting their reliability in the study of the core region, although including the core region allows us to retain the core-edge-SOL interplay without imposing arbitrary boundary conditions with the core [40].

In figure 4, typical radial profiles of electron density, temperature and pressure at the outer midplane are presented for a NT and a PT simulation with $s_{T0} = 0.025$ and $\nu_0 = 0.1$.

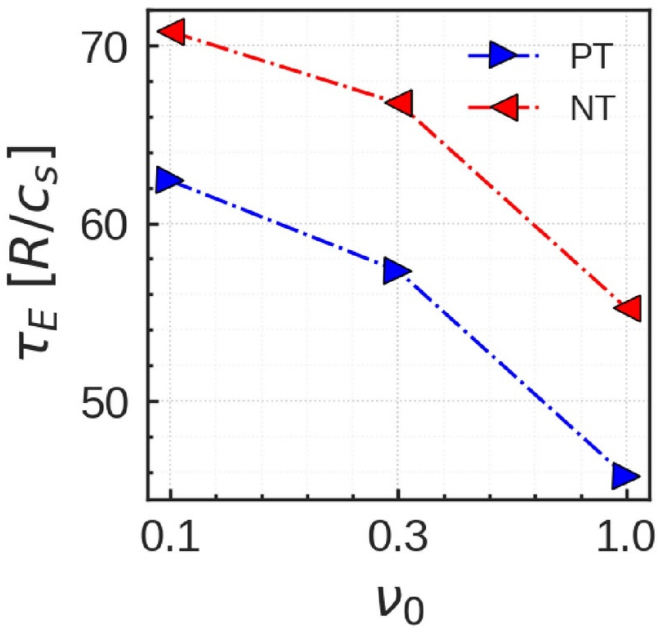


**Figure 3.** Energy confinement time $\tau_E$ as a function of $\nu_0$. The heating source is kept constant ($s_{T0} = 0.025$).

The NT configuration is characterized by steeper equilibrium gradients across the separatrix, particularly evident in the electron temperature and pressure profiles.

The steeper gradient sustained near the separatrix is associated with a larger $\boldsymbol{E}\times\boldsymbol{B}$ shear rate, $\gamma_{E\times B} = \rho_*^{-1}\partial_r^2\bar{\phi}$. In figure 5, radial profiles of the shear rate normalized to the RBM growth rate, $\gamma_{\mathrm{RBM}} = \sqrt{(2\bar{T}_e)/(\rho_* L_p)}$, where $L_p = -p/\nabla p$ is the plasma pressure gradient length in the near SOL, are shown in the proximity of the separatrix for PT and NT plasmas. The shear rate decreases as the plasma collisionality increases

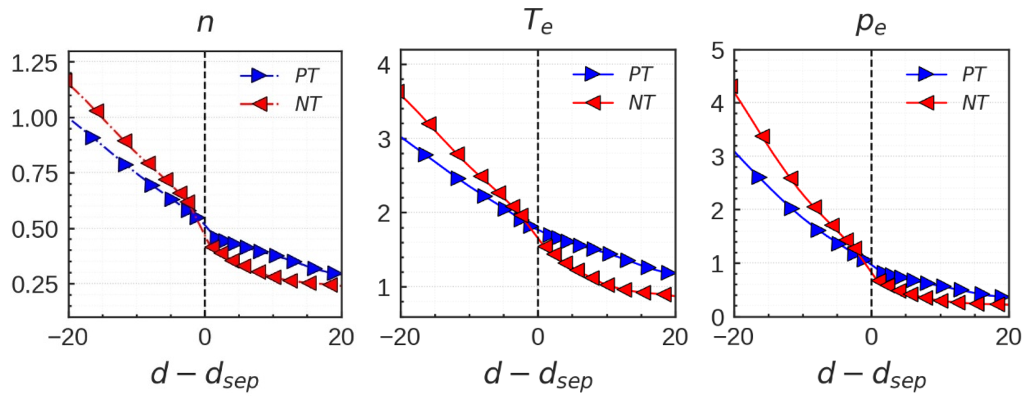


(a) Density (b) Electron temperature (c) Electron pressure

**Figure 4.** Radial profiles of density (a), electron temperature (b) and electron pressure (c) at the outer midplane for NT and PT plasmas for the simulations with $s_{T0} = 0.025$ and $\nu_0 = 0.1$.

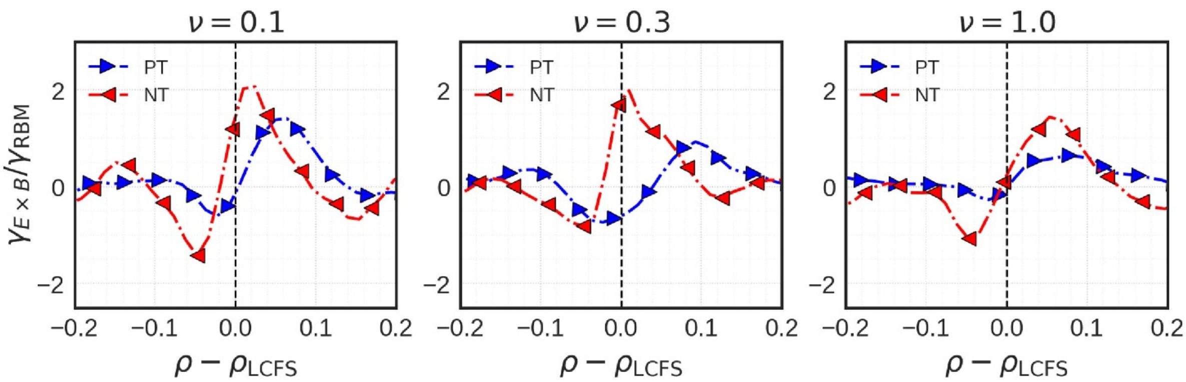


**Figure 5.** $E \times B$ shear rate normalized to $\gamma_{\mathrm{RBM}}$, the growth rate of RBMs, for a NT and a PT plasma across the separatrix. The heating source is kept constant ($s_{T0} = 0.025$).

since the high collisionality enhances the plasma transport, therefore flattening the pressure profile near the separatrix. While the normalized shear rate for the NT plasma is found to be above one in all cases, it is not sufficiently strong to create a transport barrier or destabilize a Kelvin–Helmholtz instability [52, 53].

Figure 6 shows the contour of normalized electron pressure fluctuations. While small amplitude fluctuations are observed in the core, both NT and PT plasmas display larger fluctuation amplitudes in the edge region, as well as the presence of intermittent coherent structures, known as blobs [54], in the far SOL region. Blobs are larger in size in the PT plasma. In agreement with previous results reported from simulations of limited configurations [23], NT plasmas are characterized by lower fluctuation levels and smaller eddy sizes compared to their PT counterparts. These results are in line with recent TCV experiments that point out a substantial reduction of the density, temperature fluctuation amplitude and turbulence correlation length near the edge region in NT L-mode plasmas with respect to PT discharges [11, 21].

For a qualitative analysis of the turbulent eddy size, we measure the radial extension of the turbulent structure at the low-field side (LFS), $1/k_\psi$. This is defined as the distance where the cross-correlation drops to 0.5. The radial length is then averaged in time and along the toroidal direction. The results, normalized to the tokamak minor radius, $1/(k_\psi a)$, are shown in figure 7 for PT and NT plasmas as a function of different values of collisionality. Confirming our qualitative analysis, we find that the size of turbulent eddies in NT plasmas is smaller than in PT plasmas. Furthermore, the radial size of the turbulent structure increases with plasma collisionality, indicating the presence of large-scale turbulence at high value of $\nu_0$ [54]. The typical values of $1/(k_\psi a)$ for different turbulent regimes are identified in [28], i.e. $1/(k_\psi a) \ll 1$ for RDWs and $1/(k_\psi a) \sim 0.1$ for RBMs, suggesting that the considered simulations are mainly governed by RBMs. This is confirmed by tests where we zero out the interchange drive, i.e. the curvature term in equation (2.2), and we observe a significant steepening of the pressure profile.

## 4. Estimate of the pressure gradient length

In this section, an analytical estimate of the plasma pressure gradient length in the near SOL, $L_p = -p/\nabla p$, is derived. This is correlated to the power fall-off length $\lambda_q$ that regulates the divertor heat load on the outer target [4, 30]. With the aim of predicting the SOL width as a function of the operational

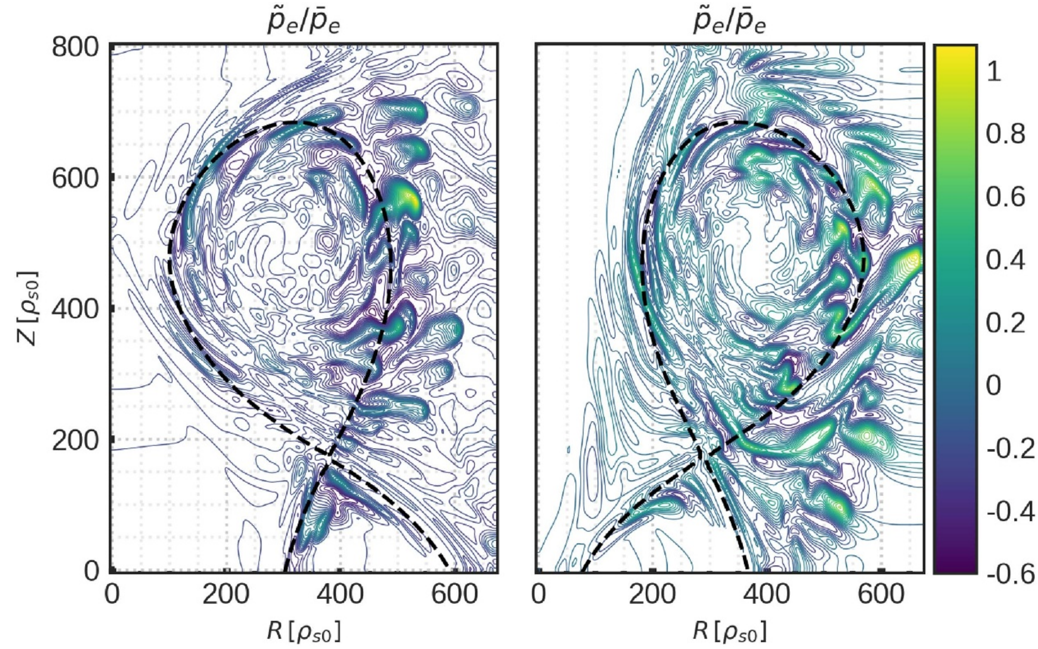


**Figure 6.** Snapshots of the fluctuating electron pressure normalized to the equilibrium electron pressure for a NT (left) and a PT (right) plasma with $s_{T0} = 0.025$ and $\nu_0 = 1.0$.

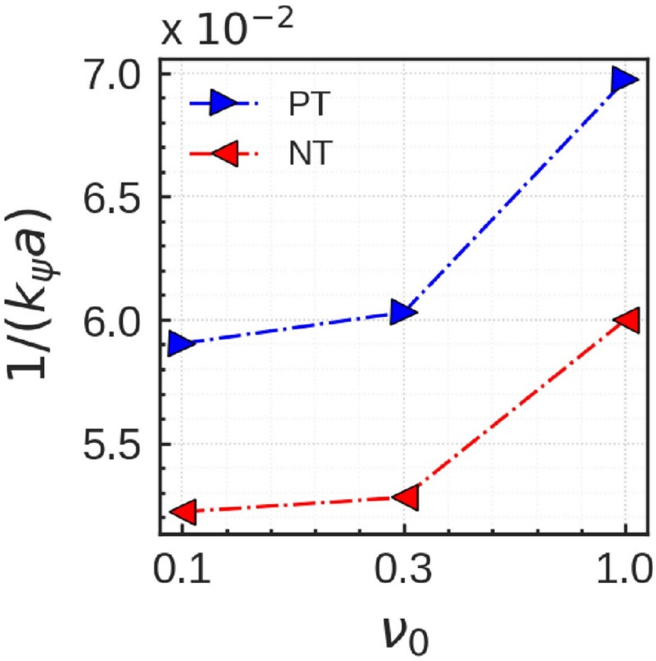


**Figure 7.** Normalized radial extension of the largest turbulent eddies at the LFS, $1/(k_\psi a)$ with $k_\psi$ being the radial wave number, is averaged in time and along the toroidal direction.

parameters, a theoretical scaling law based on the first principle approach is derived for diverted configurations in [29] leveraging previous work in limited configurations [55]. The scaling is validated against an experimental dataset for different tokamaks and nonlinear GBS simulations. Here we extend the scaling obtained in [29] to include the effects of triangularity and elongation. The derivation is based on a quasi-linear analysis, where the gradient removal mechanism [56], i.e. the local flattening of the plasma pressure profile, provides the main mechanism for the saturation of the growth of the linear instabilities driving turbulence. The value of $L_p$ is then obtained by a balance between perpendicular turbulent transport and parallel losses at the end of the magnetic field lines.

For the derivation, the flux coordinates $(x, y, z)$ introduced in section 2 are used. As the radial flux in the edge plasma is mainly driven by turbulence, it can be estimated as $\Gamma_x \sim \overline{\tilde{p}_e \partial_y \tilde{\phi}}$. The relation between $\tilde{p}_e$ and $\partial_y \tilde{\phi}$ can be obtained from the linearized electron pressure equation by combining equations (2.1) and (2.6):

$$\gamma \tilde{p}_e \sim -\frac{\rho_*^{-1}}{B}[\tilde{\phi}, \bar{p}_e] \tag{4.1}$$

$$\sim \rho_*^{-1} \partial_y \tilde{\phi} \partial_x \bar{p}_e, \tag{4.2}$$

where the curvature and parallel gradient terms are neglected by retaining only leading order contributions. The saturation of the growth instabilities occurs when their amplitude is sufficient to remove their driving gradient. Under this condition, the radial gradient associated with the pressure fluctuations is comparable to the radial gradient of the background pressure, i.e. $\tilde{p}/\bar{p} \sim 1/(k_x L_p)$ where $k_x \sim \sqrt{k_y/L_p}$ provides an estimate of the radial eddy extension, according to a non-local linear theory [57]. This allows us to express the radial flux as

$$\Gamma_x \sim \rho_* \gamma \frac{\tilde{p}_e^{\,2}}{\bar{p}_e} L_p \sim \rho_* \frac{\gamma}{k_x^2} \frac{\bar{p}_e}{L_p} \sim \rho_* \frac{\gamma}{k_y} \bar{p}_e. \tag{4.3}$$

The balance between the perpendicular turbulent transport, $\partial_x \Gamma_x \sim \Gamma_x / L_p \sim \rho_* \bar{p}_e \gamma/(k_y L_p)$, and the parallel losses at the sheath, $\nabla_\parallel(pv_{\parallel e}) \sim \rho_* \bar{p}_e c_s/q$, then leads to an estimate of the pressure scale length

$$L_p \sim \frac{q}{c_s}\left(\frac{\gamma}{k_y}\right)_{\max}. \tag{4.4}$$

In order to evaluate $(\gamma/k_y)_{\max}$ in equation (4.4), similarly to previous work [23], we linearize equations (2.1)–(2.6). For this purpose, all physical quantities are expressed as a sum of an equilibrium and a perturbation component, i.e. $n(x,y,z,t) = n_0(x) + \delta n(y,z,t)$, with $\delta n(y,z,t) = \delta n(z)\exp(ik_y y + \gamma t)$. By assuming a density equilibrium gradient, $\partial_x n = -n_0/L_n$, where $L_n = -n/\nabla n$ is the characteristic scale length, and making a similar assumption for $T_e$, while other equilibrium quantities are assumed to vanish ($\phi_0 = v_{\parallel i,0} = v_{\parallel e,0} = 0$) the linearized GBS system normalized to the separatrix value can be recast as:

$$\gamma\delta n = \frac{R_0}{L_n}\frac{1}{B}\mathcal{P}^L(\delta\phi) + \frac{2}{B}\mathcal{C}^L(\delta p_e - \delta\phi) + (\nabla_\parallel + \nabla\cdot\boldsymbol{b})(\delta j_\parallel - \delta v_{\parallel i}), \tag{4.5}$$

$$\frac{1}{B^2}\gamma\delta\omega = \frac{2}{B}\mathcal{C}^L(\delta p_e) + (\nabla_\parallel + \nabla\cdot\boldsymbol{b})\delta j_\parallel, \tag{4.6}$$

$$\frac{m_e}{m_i}\gamma\delta v_{\parallel e} = \nabla_\parallel(\delta\phi - \delta p_e - 0.71\delta T_e) + \nu\delta j_\parallel, \tag{4.7}$$

$$\gamma\delta v_{\parallel i} = -\nabla_\parallel\delta p_e, \tag{4.8}$$

$$\gamma\delta T_e = \frac{R_0}{L_n}\frac{\eta}{B}\mathcal{P}^L(\delta\phi) + \frac{4}{3B}\mathcal{C}^L\left(\delta p_e + \frac{5}{2}\delta T_e - \delta\phi\right) + \frac{2}{3}(\nabla_\parallel + \nabla\cdot\boldsymbol{b})(1.71\delta j_\parallel - \delta v_{\parallel i}), \tag{4.9}$$

where we define $\delta p_e = \delta n + \delta T_e$, $\delta j_\parallel = \delta v_{\parallel i} - \delta v_{\parallel e}$, $\delta\omega = (\nabla_\perp^2)^L\delta\phi$ and $\eta = L_n/L_{T_e}$. In addition, the linearized expressions of the geometrical operators in equations (2.30)–(2.34) can be simplified as

$$\mathcal{P}^L(f) = \mathcal{P}_{xy}\frac{\partial f}{\partial y} + \mathcal{P}_{yz}\frac{\partial f}{\partial z} \simeq i\mathcal{P}^{xy}k_y f, \tag{4.10}$$

$$\mathcal{C}^L(f) = \mathcal{C}^y\frac{\partial f}{\partial y} + \mathcal{C}^z\frac{\partial f}{\partial z} \simeq i\mathcal{C}^y k_y f, \tag{4.11}$$

$$(\nabla_\perp^2)^L f = \mathcal{N}^{yy}\frac{\partial^2 f}{\partial y^2} + \mathcal{N}^y\frac{\partial f}{\partial y} \simeq -\mathcal{N}^{yy}k_y^2 f, \tag{4.12}$$

where we neglect the relatively small $\mathcal{P}^{yz}, \mathcal{C}^z$ and $\mathcal{N}^y$ terms (see appendix A).

Provided that turbulence in our nonlinear simulations is mainly driven by RBMs in the bad curvature region, we assume a strongly localized mode at $\theta = 0$, $k_z \sim 1/q$ and $\varepsilon = 0$ to simplify equations (4.5)–(4.9). The analytical expressions of $\gamma$ and $k$ is then obtained by evaluating $\partial_{k_y}(\gamma/k_y)_{\max} = 0$ as a function of the shaping parameters [23]. As a result, the linear growth rate $\gamma$ and the poloidal wavenumber $k_y$ are given by

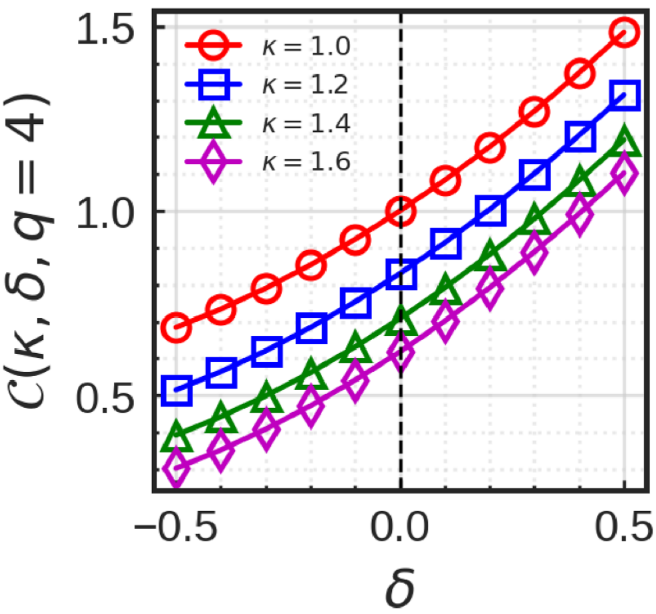


**Figure 8.** The curvature coefficient in equation (4.15), $\mathcal{C}(\kappa,\delta,q)$, at the outer midplane as a function of $\delta$ for different values of $\kappa$ with $q = 4$. The case of $\kappa = 1.0$ and $\delta = 0$ corresponds to the circular plasma, yielding $\mathcal{C}(\kappa,\delta,q) = 1$.

$$\gamma^2 = \gamma_{\text{RBM}}^2\frac{\mathcal{C}(\kappa,\delta,q)}{3}, \tag{4.13}$$

$$k_y^2 = \frac{\sqrt{3}}{2}k_{\text{RBM}}^2\mathcal{C}(\kappa,\delta,q)^{-1/2}, \tag{4.14}$$

with $\gamma_{\text{RBM}} = \sqrt{(2\bar{T}_e)/(\rho_* L_p)}$ and $k_{\text{RBM}} = 1/\sqrt{\bar{n}\nu q^2\gamma_{\text{RBM}}}$, while the effect of $\kappa$ and $\delta$ is contained in the curvature coefficient $\mathcal{C}$. This is evaluated using the fact that RBMs are mostly destabilized at the LFS. The analytical expressions of $\mathcal{C}$ at the outer midplane ($\theta = 0$) can then be approximated in the large aspect ratio limit (see appendix B)

$$\mathcal{C}(\kappa,\delta,q) = \left.\frac{\partial R_c(r,\theta)}{\partial r}\right|_{\theta=0} = 1 - \frac{\kappa-1}{\kappa+1}\frac{3q}{q+2} + \frac{\delta q}{1+q} + \frac{(\kappa-1)^2(5q-2)}{2(\kappa+1)^2(q+2)} + \frac{\delta^2}{16}\frac{7q-1}{1+q}. \tag{4.15}$$

In figure 8, the value of the curvature coefficient $\mathcal{C}(\kappa,\delta,q)$ in equation (4.15) is shown to be a function of $\kappa$ and $\delta$, while considering a safety factor constant ($q = 4$). Similar to previous results [23], $\delta$ is found to play a more important role than $\kappa$ in determining the value of $\mathcal{C}(\kappa,\delta,q)$. A similar reduction of the curvature coefficient with $\delta$ is visible also in the GBS curvature operator in appendix A.

We can now predict the value of the pressure gradient length $L_p$ as a function of the tokamak operational parameters.

We consider the balance between the heat fluxes crossing the LCFS and the volume of the integrated heat source,

$$S_p(R,Z) \simeq \oint_{\mathrm{LCFS}} q_x(R,Z)dl \sim L_\chi\, q_{x,i}, \tag{4.16}$$

where $S_p(R,Z) = \int s_p(R,Z)dRdZ$ with $s_p = ns_{T_e} + T_e s_n$, and $L_\chi = \oint_{\mathrm{LCFS}} dl$ the poloidal length of the LCFS. A common approach to obtain $L_\chi$ is to simply approximate it to the circumference of ellipse [50]. Considering that transport in the RBM regime mostly occurs at the LFS, this gives, i.e. $L_\chi \simeq \pi a\sqrt{(1+\kappa^2)/2}$. In the case of a triangular plasma, the assumption of approximating $L_\chi$ to the circumference of an ellipse leads to an error of over 10% for $|\delta| > 0.5$. To address this issue, we modify the expression for $L_\chi$ by numerically computing the poloidal length and apply a Taylor expansion around $\kappa = 1$ and $\delta = 0$. The resulting expression accounts for the effect of triangularity and can be expressed as

$$L_\chi \simeq \pi a(0.45 + 0.55\kappa) + 1.33a\delta, \tag{4.17}$$

where, the error with respect to the numerical values is found to be less than 3% when $\kappa = 1$ and $|\delta| < 0.5$.

Finally, by equating equations (4.3) and (4.16), the analytical estimate of $L_p$, including the effects of plasma shaping, can be recast as:

$$L_p \sim \mathcal{C}(\kappa,\delta,q)\left[\rho_*(\nu_0\bar{n}q^2)^2\left(\frac{L_\chi \bar{p}_e}{S_p}\right)^4\right]^{1/3}, \tag{4.18}$$

where $\mathcal{C}$ is the poloidal curvature coefficient defined in equation (4.15). Note that the above equation is equivalent to the scaling derived in [28] when the shaping term $\mathcal{C}(\kappa,\delta,q)$ is neglected.

In figure 9, the $L_p$ estimates provided by the analytical scaling law in equation (4.18) are compared with the results of the nonlinear GBS simulations presented in section 3, for different values of $\nu_0$ and $s_{T0}$. Three different values of triangularity are considered, $\delta = -0.3, 0, 0.3$. Two remarks can be made from the observation of figure 9 where good agreement is observed between the simulations and analytical results, as shown by the high $R$-square factor ($R^2 = 0.718$). First, when different values of $\delta$ with fixed $\nu_0$ and $s_{T0}$ are compared, NT plasmas tend to yield smaller values of $L_p$, mainly because of the reduction of the curvature drive. Second, when different values of $\nu_0$ and $s_{T0}$ with fixed $\delta$ are compared, we observe that the size of $L_p$ increases with $\nu_0$ and decreases with $s_{T0}$, being $L_p$ related to the size of the turbulent eddies, which increases with the plasma resistivity [28].

## 5. Comparison of $L_p$ with experimental data

In order to validate the reliability of the pressure gradient scaling law derived in section 4, a comparison against an experimental database is performed. This leverages the work in [29], where a comparison between the scaling of the pressure decay length and the experimentally measured power fall-off length $\lambda_q$ is described, showing good agreement. The database considers discharges from MAST, TCV, JET, COMPASS and Alcator C-Mod tokamaks with triangularity $0.1 < \delta < 0.5$. The scaling law considered in [29] does not take into account the effect of triangularity and can be obtained from equation (4.18) by neglecting the shaping term. However, recent works with TCV and AUG have experimentally shown that the power fall-off length at the outer target in L-mode plasmas varies by a factor of two in NT plasmas compared to PT discharges [25].

In order to carry out a comparison of the scaling in equation (4.18) with experimental results, we make use of the experimental dataset already considered for the validation in [29]. This dataset is described in [32], and includes a set of power fall-off decay lengths measured from both Langmuir probes and infrared cameras in the MAST, JET, COMPASS and Alcator C-Mod tokamaks. The discharges considered in the database are single-null L-mode plasmas in attached conditions where the pressure gradient between upstream and target is negligible. This database is expanded here by including the AUG data described in [30]. The AUG discharges include lower single-null (LSN) configurations, favorable for H-mode access, and upper single null (USN) unfavorable configurations, performed in L-mode plasmas, with triangularity $0.1 < \delta < 0.3$. In addition, we include recent TCV discharges dedicated to the study of triangularity effects on L-mode plasmas, extending our range of triangularity to $-0.3 < \delta < 0.5$.

For a direct comparison with experimental data, the scaling law in equation (4.18) is rewritten in terms of engineering parameters. By applying the same procedure as in [29], we express $S_p$ as $P_{\mathrm{SOL}}/(2\pi R_0)$ and $\nu_0$ using equation (2.9). Then equation (4.18) results into the following expression

$$L_p \simeq 1.95\,\mathcal{C}(\kappa,\delta,q)^{9/17} A^{1/17} q^{12/17} R_0^{7/17} P_{\mathrm{SOL}}^{-4/17} n_e^{10/17} \times B_T^{-12/17} L_\chi^{12/17}, \tag{5.1}$$

where we use physical units, i.e. $L_p$ [mm], $P_{\mathrm{SOL}}$ [MW], $R_0$ [m], $a$ [m], $n_e$ [$10^{19}\,\mathrm{m}^{-3}$] and $B_T$ [T]. Note that the effects of plasma shaping are included in both $\mathcal{C}(\kappa,\delta,q)$ and $L_\chi$ terms (see equations (4.15) and (4.17)).

In figure 10, we show the results of the comparison of the scaling law in equation (5.1) with the experimentally measured $\lambda_q$ at the outer target for the entire multi-machine database. Overall, very good agreement is observed with very high quality of fitting, $R^2 \simeq 0.825$ with the root-mean-square (RMS) error $\pm 1.4$ mm, where the proportionality constant $\alpha = 0.27$ is used. The newly derived scaling law for $L_p$ is found to produce a slightly better fitting result compared to the previous scaling law derived in [29], which did not include the dependence on triangularity with a value of $R^2 \simeq 0.807$. In particular, the scaling law that we propose provides better estimates for the MAST discharges [58], which is characterized by strongly shaped plasmas, approximately with $\kappa \sim 2$ and $\delta \sim 0.5$, showing larger values of $L_p$ compared to other tokamaks.

The experimental data used for the scaling law in figure 10 are found to be either in the sheath-limited regime or in the weak conduction-limited regime. This is verified by evaluating the SOL collisionality, $\nu^* = 10^{-16} n_u L/T_u^2$, for all discharges. It should be noted that the key factor that distinguishes

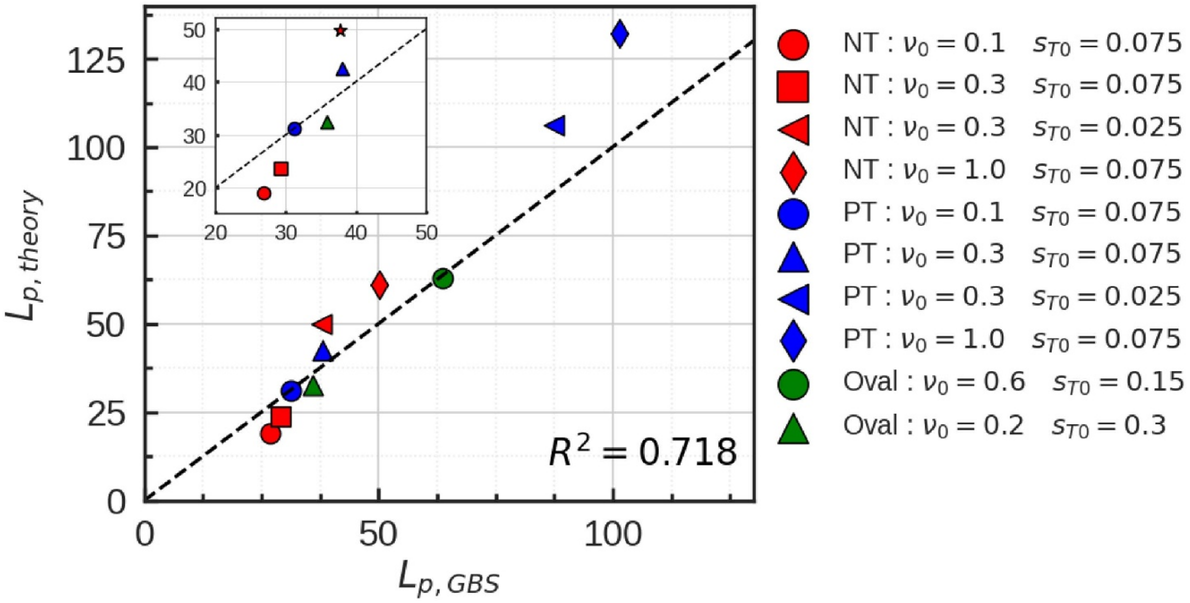


**Figure 9.** Comparison of the pressure gradient length $L_p$ between the analytical scaling law in equation (4.18) and the value of $L_p$ obtained from nonlinear GBS simulation. A parametric scan for collisionality $\nu_0$ and heating power $s_{T0}$ is carried out for different plasma shapes. Here, 'Oval' denotes elongated but non-triangular ($\delta = 0$) plasma.

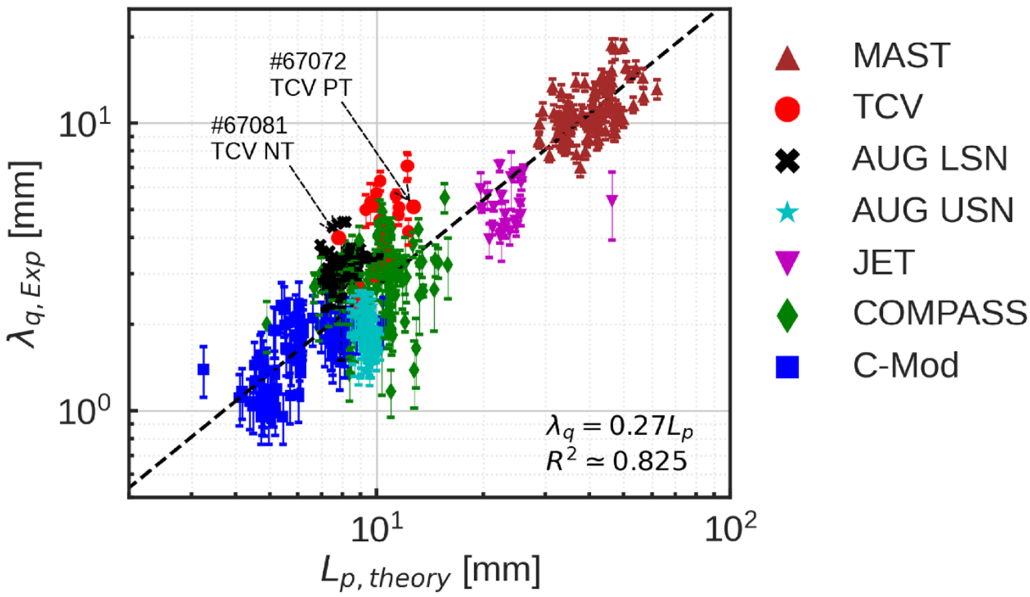


**Figure 10.** Comparison between the theoretical pressure gradient scaling law for $L_p$ by equation (5.1), and experimental power fall-off length $\lambda_q$ from multi-machine database. The fitting coefficient ($\alpha = 0.27$) is obtained using a least-squares method. The TCV experimental discharges are analyzed in the present work. We obtain a fitting quality $R^2 \simeq 0.825$.

between the sheath-limited and conduction-limited regimes is the balance between convection and conduction channels of the heat flux, along with the absence of parallel temperature gradients $\nabla_\parallel T_e$. Within this framework, the validity of the fluid model is justified even at the low $\nu^*$ conditions. The results reveal that the majority of data have $3 < \nu^* < 10$, except for a few discharges from COMPASS, TCV and AUG in the USN configuration discharges, characterized by $10 < \nu^* < 22$. Note that the AUG data for LSN (favorable) and USN (unfavorable) configurations show the effect of the toroidal magnetic field direction [59] with a larger SOL collisionality for USN ($10 < \nu^* < 13$) than the LSN discharges ($\nu^* < 10$), yielding a slight deviation from pure sheath-limited regime for USN discharges. This effect can play a role in the observed difference between LSN and USN discharges in figure 10, and will be a subject for future work.

As a further validation of our scaling law, we consider two L-mode TCV discharges with NT and PT configurations. While keeping the other TCV parameters approximately constant ($B_T = 1.43$ T, favorable ion-$\nabla B$ drift direction,

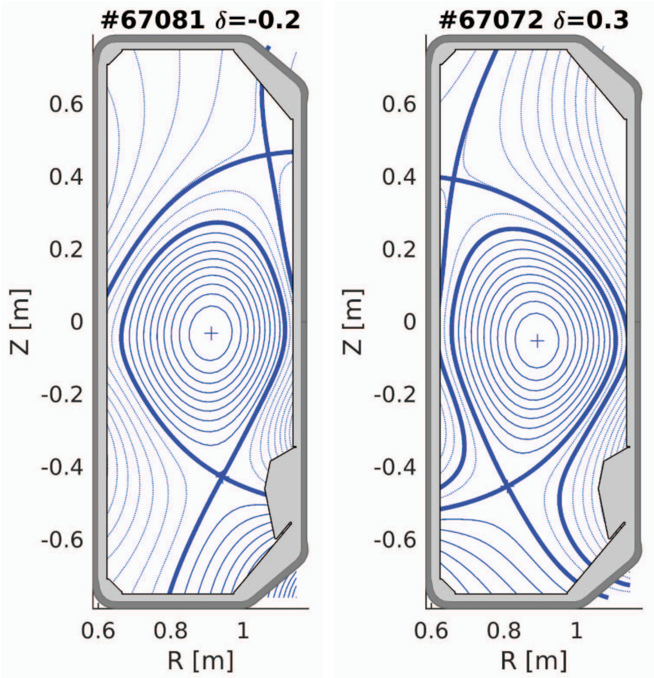


(a) NT ($\delta = -0.2$) (b) PT ($\delta = +0.3$)

**Figure 11.** The poloidal cross sections of TCV magnetic equilibria for the NT (#67081) and PT (#67072) discharges.

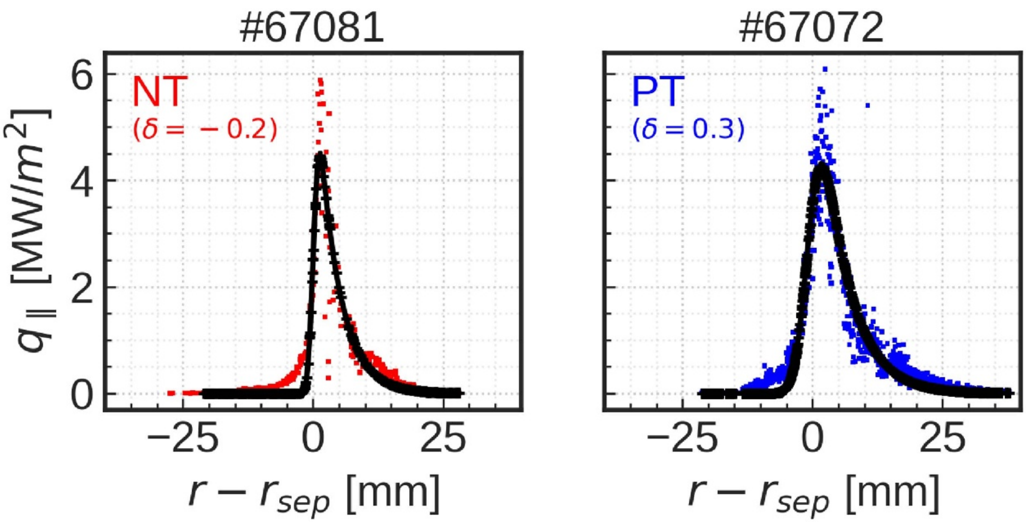


**Figure 12.** Parallel heat flux from the outer target is remapped to the outer midplane. By fitting the profile of the parallel heat flux [62] (black dashed line), the size of $\lambda_q$ is found to be ~3.99 mm for NT and ~5.12 mm for PT plasma.

plasma current $I_p = 220\,\mathrm{kA}$, line-averaged density $\langle n_e \rangle = 4 \times 10^{19}\,\mathrm{m}^{-3}$ and $\kappa = 1.5$), the value of $\delta$ is varied to investigate the effect of triangularity on the outer divertor target heat flux. In particular, we consider two discharges, which feature NT ($\delta = -0.2$) and PT ($\delta = 0.3$) magnetic equilibria, whose flux surfaces are depicted respectively in figure 11. No roll-over of the ion flux is observed, and the target peak temperature is well above 5 eV, indicating that the discharges under consideration are operating within the attached regime.

In figure 12, the parallel heat flux at the outer target, measured from Langmuir probes [60, 61], and remapped to the outer midplane, is shown for both discharges. The exponential decay length, $\lambda_q$, of the parallel heat flux is evaluated by using the so-called Eich-fit [62], defined as:

$$q(\bar{r}) = \frac{q_0}{2} \exp\left[\left(\frac{S}{2\lambda_q}\right)^2 - \frac{\bar{r}}{\lambda_q}\right] \cdot \mathrm{erfc}\left(\frac{S}{2\lambda_q} - \frac{\bar{r}}{S}\right) \quad (5.2)$$

where $\bar{r} = r - r_{\mathrm{sep}}$ is the upstream coordinate, $S$ is the divertor broadening, and $q_0$ is the peak heat flux at the strike position.

The scatter of the data leads to a relatively large uncertainty in the fit, yielding an estimate of $\lambda_{q,\mathrm{NT}} = 3.99 \pm$

**Table 1.** Power fall-off length extrapolation of future tokamaks for NT and PT L-mode plasmas. The values of $\lambda_{q,\mathrm{NT}}$ are computed using an opposite value of triangularity, $-\delta$, in the scaling law.

| Parameter | ITER | DTT | SPARC | JT-60SA |
|---|---|---|---|---|
| $R_0$ (m) | 6.2 | 2.1 | 1.85 | 2.96 |
| $a$ (m) | 2 | 0.6 | 0.57 | 1.18 |
| $q_{95}$ | 3 | 3 | 3 | 3 |
| $\kappa$ | 1.85 | 1.7 | 1.97 | 1.95 |
| $\delta$ | 0.49 | 0.3 | 0.54 | 0.53 |
| $\bar{n}_e(\mathrm{m}^{-3})$ | $4\times10^{19}$ | $1.8\times10^{20}$ | $3.1\times10^{20}$ | $6.3\times10^{19}$ |
| $B_T$ (T) | 5.3 | 6 | 12.2 | 2.3 |
| $P_{\mathrm{SOL}}$ (MW) | 18 | 15 | 29 | 10 |
| $\lambda_{q,\mathrm{PT}}$ (mm) | $\sim$4.7 | $\sim$2.6 | $\sim$2.1 | $\sim$6.8 |
| $\lambda_{q,\mathrm{NT}}$ (mm) | $\sim$2 | $\sim$1.5 | $\sim$0.8 | $\sim$2.6 |

0.42 (mm) and $\lambda_{q,\mathrm{PT}} = 5.12 \pm 0.36$ (mm). The $\lambda_{q,\mathrm{NT}}$ plasmas appears to be smaller than approximately $\sim$20% than the $\lambda_{q,\mathrm{PT}}$. This is qualitatively in agreement with the $L_p$ scaling law in equation (4.18), which predicts $\lambda_{q,\mathrm{NT}} \simeq 1.6 \pm 0.5$ mm and $\lambda_{q,\mathrm{PT}} \simeq 2.7 \pm 0.8$ mm, using the proportionality constant $\alpha = 0.27$ found in the analysis of the multi-machine database. The theoretical scaling law reproduces the increase of $\lambda_q$ proportional to $\delta$, with an error comparable to the RMS error found in the analysis of the multi-machine database (we note that, in the analysis multi-machine in figure 10, larger experimental $L_p$ than the theoretical scaling is observed for the TCV tokamak). The theoretical prediction we provide is accompanied by an error bar that reflects the uncertainty in the power entering the SOL, specifically the radiative power. Furthermore, the difference between the scaling law and the experimental measurement can be attributed to the use of the global value of $\delta$, instead of distinguishing between $\delta_{\mathrm{upper}}$ and $\delta_{\mathrm{lower}}$ [25].

The derived scaling law can be used to predict the SOL width in future devices. In table 1, the SOL power fall-off length $\lambda_q$ predictions provided by equation (5.1) for future tokamaks, such as ITER [63] (the scenario obtained from METIS simulations [64] just before the L-H transition is considered), DTT [65], SPARC [66] and JT-60SA [67], are listed assuming operations in L-mode and a triangularity value based on their baseline scenario. These tokamaks consider baseline scenarios operating in a PT configuration. As a comparison, we also report the expected $\lambda_q$ value in NT, with opposite triangularity than the baseline scenario. In particular, we note that the predicted $\lambda_q$ in ITER for NT L-mode plasma yield $\lambda_q \simeq 2$ mm, which is twice as large as the predicted $\lambda_q \sim 1$ mm for the H-mode burning plasma scenario [68], highlighting the attractiveness of NT L-mode plasma in terms of handling the exhaust of the divertor targets, in addition to the advantage of operating ELM-free scenarios [69].

## 6. Conclusions

In the present paper, the effects of triangularity on boundary plasma turbulence are investigated using global, flux-driven, two-fluid GBS simulations. A first-principles theoretical scaling law for the SOL width including triangularity is derived based on considerations of the linear growth rate and nonlinear saturation mechanisms of the driving instabilities. Overall, plasma shaping parameters are found to be important elements in determining the properties of boundary plasma turbulencein particular, the power fall-off length $\lambda_q$.

A series of nonlinear GBS simulations is carried out for NT and PT L-mode diverted plasmas. NT plasmas show stabilizing effects on edge plasma turbulence yielding (i) higher electron equilibrium pressure, (ii) reduced eddy size, (iii) steeper plasma gradient at the separatrix and (iv) improved energy confinement, with respect to PT simulations. Turbulence stabilization is due to the reduction of the magnetic curvature drive. Indeed, the curvature operator is found to decrease at the LFS for an elongated NT plasma resulting into stabilized SOL plasma turbulence, especially when RBM is the driving instability.

Leveraging the analysis of the simulation results and as an extension of the previous work in [29], a theoretical scaling law for $L_p$ is derived to include the effect of triangularity in the $L_p$ estimate. The scaling law is then compared to the results of GBS simulations. The linear analysis shows a weak growth rate and a higher value of the poloidal wavenumber $k_y$ (poloidally decorrelated turbulence structure) in an elongated NT plasma. A comparison of the theoretical scaling with the results of a set of GBS simulations at different collisionality and input power shows an overall good agreement, with the analytical scaling, correctly capturing the $L_p$ reduction observed in NT GBS simulations. The above results are consistent with the experimental work reported in [25].

To validate our scaling law, a comparison between the theory-based $L_p$ scaling law and experimental $\lambda_q$ dataset from different tokamaks is successfully performed. The newly derived scaling law captures the decrease of $\lambda_q$ in NT plasmas, and the quality of fitting is found to be slightly improved compared to the scaling law, which did not take into account the dependence on triangularity. Finally, we carried out predictions of the SOL width in future devices, assuming operations in L-mode plasmas. The predicted $\lambda_q$ values for NT L-mode plasmas are larger than those for PT H-mode scenarios (table 1). Overall, the results are consistent with the experimental work reported in [25], indicating that NT plasmas can be an attractive option for power handling in ELM-free scenarios.

## Data availability statement

The data cannot be made publicly available upon publication because no suitable repository exists for hosting data in this field of study. The data that support the findings of this study are available upon reasonable request from the authors.

## Acknowledgments

The authors acknowledge T Eich as well as the participants of the Festival de Théorie 2022, Aix-en-Provence, for helpful discussions. This work has been carried out within the framework of the EUROfusion Consortium, partially funded by the European Union via the Euratom Research and Training Programme (Grant Agreement No. 101052200—EUROfusion). The Swiss contribution to this work has been funded by the Swiss State Secretariat for Education, Research and Innovation (SERI). Views and opinions expressed are however those of the author(s) only and do not necessarily reflect those of the European Union, the European Commission or SERI. Neither the European Union nor the European Commission nor SERI can be held responsible for them. The simulations presented herein were carried out in part on the CINECA Marconi supercomputer under the TSVV-1 and TSVV-2 project and in part at CSCS (Swiss National Supercomputing Center).

## Appendix A. Geometrical coefficients and differential operators

We deduce the expressions of the geometrical coefficients presented in equations (2.30)–(2.34). Introducing the cylindrical coordinate system $\boldsymbol{R} = (R_c(r,\theta), \varphi_c, Z_c(r,\theta))$, the covariant metric tensor in the $(r,\theta,\varphi)$ coordinates are given by

$$g_{rr} = \left(\frac{\partial R_c}{\partial r}\right)^2 + \left(\frac{\partial Z_c}{\partial r}\right)^2, \tag{A.1}$$

$$g_{\theta r} = \frac{\partial R_c}{\partial r}\frac{\partial R_c}{\partial \theta} + \frac{\partial Z_c}{\partial r}\frac{\partial Z_c}{\partial \theta}, \tag{A.2}$$

$$g_{\theta\theta} = \left(\frac{\partial R_c}{\partial \theta}\right)^2 + \left(\frac{\partial Z_c}{\partial \theta}\right)^2, \tag{A.3}$$

$$g_{\varphi\varphi} = R_c^2, \tag{A.4}$$

$$g_{r\varphi} = g_{\theta\varphi} = 0, \tag{A.5}$$

where we use the definition of the metric coefficients

$$g_{ij} = \boldsymbol{e}_i \cdot \boldsymbol{e}_j = \frac{\partial \boldsymbol{R}}{\partial \xi_i} \cdot \frac{\partial \boldsymbol{R}}{\partial \xi_j}, \tag{A.6}$$

with $\boldsymbol{\xi} = (r,\theta,\varphi) = (\xi_1,\xi_2,\xi_3)$.

The contravariant metric tensors in $(r,\theta,\varphi)$ coordinates are obtained by inverting the covariant metric tensors. By using the relation given by

$$g^{ij} = g^{mn}\frac{\partial u_i}{\partial u^m}\frac{\partial u^j}{\partial u^n}, \tag{A.7}$$

the contravariant metric tensor in flux-tube coordinates $(r,\alpha,\theta_*)$, where $\alpha = \varphi - q(r)\theta_*$ is a field line label and $\theta_*$ is the straight-field-line angle defined in equation (2.28), can then be obtained. The resulting expressions can be recast as

$$g^{\theta_*\theta_*} = \left(\frac{\partial \theta_*}{\partial \theta}\right)^2 g^{\theta\theta} + 2\frac{\partial \theta_*}{\partial \theta}\frac{\partial \theta_*}{\partial \theta} g^{\theta r} + \left(\frac{\partial \theta_*}{\partial r}\right)^2 g^{rr}, \tag{A.8}$$

$$g^{\theta_* r} = \frac{\partial \theta_*}{\partial r} g^{rr} + \frac{\partial \theta_*}{\partial \theta} g^{\theta r}, \tag{A.9}$$

$$g^{r\theta_*} = \frac{\partial \theta_*}{\partial r} g^{rr} + \frac{\partial \theta_*}{\partial \theta} g^{r\theta}, \tag{A.10}$$

$$g^{\theta_*\alpha} = -s(r)\theta_*\frac{q(r)}{r} g^{\theta_* r} - q(r) g^{\theta_*\theta_*}, \tag{A.11}$$

$$g^{r\alpha} = -s(r)\theta_*\frac{q(r)}{r} g^{rr} - q(r) g^{\theta_* r}, \tag{A.12}$$

$$g^{\alpha\alpha} = g^{\varphi\varphi} + q(r)^2 g^{\theta_*\theta_*} + 2\frac{q(r)^2 s(r)\theta_*}{r} g^{\theta_* r} + [s(r)\theta_*]^2\frac{q(r)^2}{r^2} g^{rr}, \tag{A.13}$$

where $s(r) = (r/q)(dq/dr)$ is the magnetic shear.

By using the analytical expressions of the metric tensors defined in equations (A.8)–(A.13), the geometrical coefficients presented in equations (2.30)–(2.34) can be analytically expressed in the re-scaled flux-tube coordinate system $x = r, y = (a/q)\alpha, z = qR_0\theta_*$ leading to

$$\mathcal{P}_{xy} = -\frac{b_{\theta_*} a}{\mathcal{J} q}, \quad \mathcal{P}_{yz} = -\frac{a b_r}{\mathcal{J}}, \quad \mathcal{P}_{zx} = -\frac{q b_\alpha}{\mathcal{J}}, \tag{A.14}$$

$$\mathcal{D}^x = \mathcal{D}^y = 0, \quad \mathcal{D}^z = qR_0 b^{\theta_*}, \tag{A.15}$$

$$\mathcal{C}^x = -\frac{R_0 B}{2\mathcal{J}}\frac{\partial c_\alpha}{\partial \theta_*}, \quad \mathcal{C}^y = \frac{aR_0 B}{2\mathcal{J} q}\left(\frac{\partial c_r}{\partial \theta_*} - \frac{\partial c_{\theta_*}}{\partial r}\right), \quad \mathcal{C}^z = \frac{qR_0 B}{2\mathcal{J}}\frac{\partial c_\alpha}{\partial r}, \tag{A.16}$$

$$\mathcal{N}^{xx} = g^{rr}, \quad \mathcal{N}^{xy} = \frac{2g^{\alpha r} a}{q}, \quad \mathcal{N}^{yy} = \frac{a^2 g^{\alpha\alpha}}{q^2}, \tag{A.17}$$

$$\mathcal{N}^x = \nabla^2 r, \quad \mathcal{N}^y = \frac{a}{q}\nabla^2\alpha,$$
$$\mathcal{N}^z = qR_0\left(\nabla^2\theta_* - \frac{1}{\mathcal{J}}\frac{\partial}{\partial\theta_*}[\mathcal{J}(b^{\theta_*})^2]\right), \tag{A.18}$$

$$\mathcal{N}^{xz} = 2qg^{r\theta_*}, \quad \mathcal{N}^{yz} = 2ag^{\theta_*\alpha}, \quad \mathcal{N}^{zz} = q^2[g^{\theta_*\theta_*} - (b^{\theta_*})^2], \tag{A.19}$$

where $c_i = b_i/B$.

Due to the fact that the scale length of the turbulence along the radial direction is larger than along the poloidal direction ($k_y \gg k_x$) and that the parallel turbulence wavelengths is such that ($k_z \ll 1$), the operators in equations (2.30)–(2.34) can be further simplified. For example, the curvature operator in flux-tube coordinates can be written as

$$\mathcal{C}(f) = \mathcal{C}^x\frac{\partial f}{\partial x} + \mathcal{C}^y\frac{\partial f}{\partial y} + \mathcal{C}^z\frac{\partial f}{\partial z} \simeq \mathcal{C}^y\frac{\partial A}{\partial y}. \tag{A.20}$$

## Appendix B. Derivation of the curvature operator

An analytical expression of the magnetic equilibrium for arbitrary values of $\kappa$ and $\delta$ can be obtained by solving the Grad–Shafranov equation in the large aspect ratio limit $\epsilon = r/R_0 \to 0$, when the plasma pressure contribution is neglected [23, 70, 71]. By keeping the zeroth and first order terms in $\varepsilon$, the magnetic equilibrium takes the following form [71]

$$R_c(r,\theta) = R_0\left[1 + \epsilon\cos\theta + \sum_{m=2}^{3}\frac{S_m(r)}{R_0}\cos[(m-1)\theta] - \frac{1-m}{2\epsilon}\left(\frac{S_m(r)}{R_0}\right)^2\cos\theta\right], \tag{B.1}$$

$$Z_c(r,\theta) = R_0\left[\epsilon\sin\theta - \sum_{m=2}^{3}\frac{S_m(r)}{R_0}\sin[(m-1)\theta] - \frac{1-m}{2\epsilon}\left(\frac{S_m(r)}{R_0}\right)^2\sin\theta\right], \tag{B.2}$$

where the functions $S_2(r), S_3(r)$ are related to the shaping parameters

$$\kappa = \frac{a - S_2(a)}{a + S_2(a)} \tag{B.3}$$

and

$$\delta = \frac{4S_3(a)}{a}. \tag{B.4}$$

By assuming a strongly localized RBM at $\theta = 0$, it is possible to approximate the curvature operator as $\mathcal{C}^y \simeq -\partial_r R_c(r,\theta)\big|_{\theta=0} = -\partial_r R_c(r,0) - \partial_\theta R_c(r,0)\partial_r\theta\big|_{\theta_*=0}$. Then, using the fact that $\partial_r\theta\big|_{\theta_*=0} = 0$ for $\varepsilon = 0$, the curvature coefficient at the LCFS, $r = a$, can be recast as

$$\mathcal{C}(\kappa,\delta,q) = \frac{\partial R_c(r,\theta)}{\partial r}\bigg|_{\theta_*=0} = 1 + \sum_{m=2}^{3}S'_m(a) - \sum_{m=2}^{3}\frac{1-m}{a}\left[S_m(a)S'_m(a) - \frac{S_m(a)^2}{2a}\right]. \tag{B.5}$$

The expressions for $S_m(r)$ and $q(r)$ are given by

$$S_m(r) = S_m(a)\left(\frac{r}{a}\right)^{m-1}\frac{q(r)s(r) + 2q_0\frac{m+1}{m-1}}{qs + 2q_0\frac{m+1}{m-1}}, \tag{B.6}$$

$$q(r) = q_0 + (q - q_0)\left(\frac{r}{a}\right)^2, \tag{B.7}$$

where $q_0$ is the safety factor measured on the magnetic axis. For $m = 2, 3$ and $r = a$, the shaping term and its derivatives can be written as

$$\frac{S_2(a)}{a} = -\frac{\kappa - 1}{\kappa + 1}, \tag{B.8}$$

$$\frac{S_3(a)}{a} = \frac{\delta}{4} \tag{B.9}$$

and

$$S'_2(a) = -\left(\frac{\kappa-1}{\kappa+1}\right)\left(\frac{3q}{q+2}\right), \tag{B.10}$$

$$S'_3(a) = \frac{\delta q}{q+1}. \tag{B.11}$$

Finally, by inserting the expressions of $S_m(r)$ and $S'_m(r)$ for $m = 2, 3$ into equation (B.5), the curvature coefficient at $\theta = 0$ leads to

$$\mathcal{C}(\kappa,\delta,q) = 1 - \frac{\kappa-1}{\kappa+1}\frac{3q}{q+2} + \frac{\delta q}{1+q} + \frac{(\kappa-1)^2(5q-2)}{2(\kappa+1)^2(q+2)} + \frac{\delta^2}{16}\frac{7q-1}{1+q}. \tag{B.12}$$

## ORCID iDs

K Lim https://orcid.org/0000-0002-0174-2300
M Giacomin https://orcid.org/0000-0003-2821-2008
A Coelho https://orcid.org/0000-0002-8889-7259
O Février https://orcid.org/0000-0002-9290-7413
D Silvagni https://orcid.org/0000-0003-2103-3592

## References


[1] JET Design Group 1973 The JET project—preliminary description (EUR-JET-R1) Abingdon: Culham Laboratory

[2] Lazarus E A *et al* 1991 Higher beta at higher elongation in the DIII-D tokamak *Phys. Fluids* B **3** 2220–9

[3] Miura Y Takizuka T, Tamai H, Matsuda T, Suzuki N, Mori M, Maeda H, Itoh K, Itoh S I and Kardaun O J W F 1992 Geometric dependence of the energy confinement time scaling for H-mode discharges *Nucl. Fusion* **32** 1473

[4] Loarte A *et al* 2007 Chapter 4: Power and particle control *Nucl. Fusion* **47** S203

[5] Eich T, Sieglin B, Thornton A J, Faitsch M, Kirk A, Herrmann A and Suttrop W 2017 ELM divertor peak energy fluence scaling to ITER with data from JET, MAST and ASDEX upgrade *Nucl. Mater. Energy* **12** 84

[6] Kikuchi M *et al* 2019 L-mode-edge negative triangularity tokamak reactor *Nucl. Fusion* **59** 056017

[7] Weisen H *et al* 1997 Effect of plasma shape on confinement and MHD behaviour in the TCV tokamak *Nucl. Fusion* **37** 1741

[8] Pochelon A *et al* 1999 Energy confinement and MHD activity in shaped TCV plasmas with localized electron cyclotron heating *Nucl. Fusion* **39** 1807

[9] Camenen Y Pochelon A, Behn R, Bottino A, Bortolon A, Coda S, Karpushov A, Sauter O and Zhuang G (the TCV team) 2007 Impact of plasma triangularity and collisionality on electron heat transport in TCV L-mode plasmas *Nucl. Fusion* **47** 510

[10] Fontana M, Porte L, Coda S and Sauter O 2018 The effect of triangularity on fluctuations in a tokamak plasma *Nucl. Fusion* **58** 024002

[11] Huang Z and Coda S (the TCV team) 2019 Dependence of density fluctuations on shape and collisionality in positive- and negative-triangularity tokamak plasmas *Plasma Phys. Control. Fusion* **61** 014921

[12] Fontana M, Porte L, Coda S, Sauter O, Brunner S, Jayalekshmi A C, Fasoli A and Merlo G 2020 Effects of collisionality and $T_e/T_i$ on fluctuations in positive and negative tokamak plasmas *Nucl. Fusion* **60** 016006

[13] Coda S *et al* 2022 Enhanced confinement in diverted negative-triangularity L-mode plasmas in TCV *Plasma Phys. Control. Fusion* **64** 014004

[14] Austin M E *et al* 2019 Achievement of reactor-relevant performance in negative triangularity shape in the DIII-D tokamak *Phys. Rev. Lett.* **122** 115001

[15] Marinoni A *et al* 2019 H-mode grade confinement in L-mode edge plasmas at negative triangularity on DIII-D *Phys. Plasmas* **26** 042515

[16] Marinoni A *et al* 2021 Diverted negative triangularity plasmas on DIII-D: the benefit of high confinement without the liability of an edge pedestal *Nucl. Fusion* **61** 116010

[17] Happel T Pütterich T, Told D, Dunne M, Fischer R, Hobirk J, McDermott R M and Plank U (ASDEX Upgrade Team the) 2023 Overview of initial negative triangularity plasma studies on the ASDEX Upgrade tokamak *Nucl. Fusion* **63** 016002

[18] Marinoni A, Brunner S, Camenen Y, Coda S, Graves J P, Lapillonne X, Pochelon A, Sauter O and Villard L 2009 The effect of plasma triangularity on turbulent transport: modeling TCV experiments by linear and non-linear gyrokinetic simulations *Plasma Phys. Control. Fusion* **51** 055016

[19] Wan W, Chen Y, Parker S and Groebner R J 2015 Effects of the magnetic equilibrium on gyrokinetic simulations of tokamak microinstabilities *Phys. Plasmas* **22** 062502

[20] Merlo G, Fontana M, Coda S, Hatch D, Janhunen S, Porte L and Jenko F 2019 Turbulent transport in TCV plasmas with positive and negative triangularity *Phys. Plasmas* **26** 102302

[21] Merlo G *et al* 2021 Nonlocal effects in negative triangularity TCV plasmas *Plasma Phys. Control. Fusion* **63** 044001

[22] Duff J M, Faber B J, Hegna C C, Pueschel M J and Terry P W 2022 Effect of triangularity on ion-temperature-gradient-driven turbulence *Phys. Plasmas* **29** 012303

[23] Riva F, Lanti E, Jolliet S and Ricci P 2017 Plasma shaping effects on tokamak scrape-off layer turbulence *Plasma Phys. Control. Fusion* **59** 035001

[24] Laribi E, Serre E, Tamain P and Yang H 2021 Impact of negative triangularity on edge plasma transport and turbulence in TOKAMAK3X simulations *Nucl. Mater. Energy* **27** 101012

[25] Faitsch M Maurizio R, Gallo A, Coda S, Eich T, Labit B, Merle A, Reimerdes H, Sieglin B and Theiler C 2018 Dependence of the L-Mode scrape-off layer power fall-off length on the upper triangularity in TCV *Plasma Phys. Control. Fusion* **60** 045010

[26] Han W, Offeddu N, Golfinopoulos T, Theiler C, Tsui C K, Boedo J A and Marmar E S (the TCV Team) 2021 Suppression of first-wall interaction in negative triangularity plasmas on TCV *Nucl. Fusion* **61** 034001

[27] Riva F, Tsui C K, Boedo J A and Ricci P 2020 Shaping effects on scrape-off layer plasma turbulence: a rigorous validation of three-dimensional simulations against TCV measurements *Phys. Plasmas* **27** 012301

[28] Giacomin M and Ricci P 2020 Investigation of turbulent transport regimes in the tokamak edge by using two-fluid simulations *J. Plasma Phys.* **86** 905860502

[29] Giacomin M, Stagni A, Ricci P, Boedo J A, Horacek J, Reimerdes H and Tsui C K 2021 Theory-based scaling laws of near and far scrape-off layer widths in single-null L-mode discharges *Nucl. Fusion* **61** 076002

[30] Silvagni D, Eich T, Faitsch M, Happel T, Sieglin B, David P, Nille D, Gil L and Stroth U 2020 Scrape-off layer (SOL) power width scaling and correlation between SOL and pedestal gradients across L, I and H-mode plasmas at ASDEX Upgrade *Plasma Phys. Control. Fusion* **62** 045015

[31] Brunner D, LaBombard B, Kuang A Q and Terry J L 2018 High-resolution heat flux width measurements at reactor-level magnetic fields and observation of a unified width scaling across confinement regimes in the Alcator C-Mod tokamak *Nucl. Fusion* **58** 094002

[32] Horacek J *et al* 2020 Scaling of L-mode heat flux for ITER and COMPASS-U divertors, based on five tokamaks *Nucl. Fusion* **60** 066016

[33] Scarabosio A, Eich T, Herrmann A and Sieglin B 2013 Outer target heat fluxes and power decay length scaling in L-mode plasmas at JET and AUG *J. Nucl. Mater.* **438** S426–30

[34] Ahn J-W, Counsell G F and Kirk A 2006 L-mode SOL width scaling in the MAST spherical tokamak *Plasma Phys. Control. Fusion* **48** 1077

[35] Stangeby P M 2000 *The Plasma Boundary of Magnetic Fusion Devices* (Bristol: CRC Press) (https://doi.org/10.1201/9780367801489)

[36] Zeiler A, Drake J F and Rogers B 1997 Nonlinear reduced Braginskii equations with ion thermal dynamics in toroidal plasma *Phys. Plasmas* **4** 2134

[37] Rogers B N and Ricci P 2013 Low-frequency turbulence in a linear magnetized plasma *Phys. Rev. Lett.* **104** 225002

[38] Ricci P Halpern F D, Jolliet S, Loizu J, Mosetto A, Fasoli A, Furno I and Theiler C 2012 Simulation of plasma turbulence in scrape-off layer conditions: the GBS code, simulation results and code validation *Plasma Phys. Control. Fusion* **54** 124047

[39] Halpern F C, Ricci P, Jolliet S, Loizu J, Morales J, Mosetto A, Musil F, Riva F, Tran T M and Wersal C 2016 The GBS code for tokamak scrape-off layer simulations *J. Comput. Phys.* **315** 388

[40] Giacomin M, Ricci P, Coroado A, Fourestey G, Galassi D, Lanti E, Mancini D, Richart N, Stenger L N and Varini N 2022 The GBS code for the self-consistent simulation of plasma turbulence and kinetic neutral dynamics in the tokamak boundary *J. Comput. Phys.* **463** 111294
[41] Paruta P, Ricci P, Riva F, Wersal C, Beadle C and Frei B 2018 Simulation of plasma turbulence in the periphery of diverted tokamak by using the GBS code *Phys. Plasmas* **25** 112301
[42] Beadle C and Ricci P 2020 Understanding the turbulent mechanisms setting the density decay length in the tokamak scrape-off layer *J. Plasma Phys.* **86** 175860101
[43] Giacomin M, Stenger L N and Ricci P 2020 Turbulence and flows in the plasma boundary of snowflake magnetic configurations *Nucl. Fusion* **60** 024001
[44] Coelho A, Loizu J, Ricci P and Giacomin M 2022 Global fluid simulation of plasma turbulence in a stellarator with an island divertor *Nucl. Fusion* **62** 074004
[45] Wersal C and Ricci P 2015 A first-principles self-consistent model of plasma turbulence and kinetic neutral dynamics in the tokamak scrape-off layer *Nucl. Fusion* **55** 123014
[46] Giacomin M and Ricci P 2022 Turbulent transport regimes in the tokamak boundary and operational limits *Phys. Plasmas* **29** 062303
[47] D'haeseleer W D, Hitchon W N G, Callen J D and Shohet J L 1991 *Flux Coordinates and Magnetic Field Structure* (Berlin: Springer) (https://doi.org/10.1007/978-3-642-75595-8)
[48] Loizu J, Ricci P, Halpern F D and Jolliet S 2012 Boundary conditions for plasma fluid models at the magnetic presheath entrance *Phys. Plasmas* **19** 122307
[49] Reimerdes H *et al* 2013 Overview of the TCV tokamak experimental programme *Nucl. Fusion* **62** 042018
[50] Sauter O 2016 Geometric formulas for system codes including the effect of negative triangularity *Fusion Eng. Des.* **112** 633
[51] Scott B 1997 Three-dimensional computation of drift Alfvén turbulence *Plasma Phys. Control. Fusion* **39** 1635
[52] Rogers B N and Dorland W 2005 Noncurvature-driven modes in a transport barrier *Phys. Plasmas* **12** 062511
[53] Myra J R, D'Ippolito D A, Russell D A, Umansky M V and Baver D A 2016 Analytical and numerical study of the transverse Kelvin–Helmholtz instability in tokamak edge plasmas *J. Plasma Phys.* **82** 905820210
[54] D'Ippolito D A, Myra J R and Zweben S J 2011 Convective transport by intermittent blob-filaments: comparison of theory and experiment *Phys. Plasmas* **18** 060501
[55] Halpern F D *et al* 2013 Theory-based scaling of the SOL width in circular limited tokamak plasmas *Nucl. Fusion* **53** 122001
[56] Ricci P and Rogers B N 2013 Plasma turbulence in the scrape-off layer of tokamak devices *Phys. Plasmas* **20** 010702
[57] Ricci P, Rogers B N and Brunner S 2008 High- and low-confinement modes in simple magnetized toroidal plasmas *Phys. Rev. Lett.* **100** 225002
[58] Sykes A *et al* 2001 First results from MAST *Nucl. Fusion* **41** 1423
[59] Faitsch M, Sieglin B, Eich T, Sun H J and Herrmann A (the ASDEX Upgrade Team) 2015 Change of the scrape-off layer power width with the toroidal B-field direction in ASDEX upgrade *Plasma Phys. Control. Fusion* **57** 075005
[60] Février O, Theiler C, De Oliveira H, Labit B, Fedorczak N and Baillod A 2018 Analysis of wall-embedded Langmuir probe signals in different conditions on the Tokamak à Configuration Variable *Rev. Sci. Instrum.* **89** 053502
[61] De Oliveira H, Marmillod P, Theiler C, Chavan R, Février O, Labit B, Lavanchy P, Marlétaz B and Pitts R A (TCV team) 2019 Langmuir probe electronics upgrade on the tokamak à configuration variable *Rev. Sci. Instrum.* **90** 083502
[62] Eich T, Sieglin B, Scarabosio A, Fundamenski W, Goldston R J and Herrmann A 2011 Inter-ELM power decay length for JET and ASDEX upgrade: measurement and comparison with heuristic drift-based model *Phys. Rev. Lett.* **107** 215001
[63] Campbell D J 2016 The first fusion reactor: ITER *Europhys. News* **47** 28
[64] Artaud J F *et al* 2018 Metis: a fast integrated tokamak modelling tool for scenario design *Nucl. Fusion* **58** 105001
[65] Martone R *et al* 2019 *DTT Divertor Tokamak Test facility—Interim Design Report* ENEA (available at: www.dtt-project.it/DTT_IDR_2019_WEB.pdf)
[66] Rodriguez-Fernandez P *et al* 2020 Overview of the SPARC physics basis towards the exploration of burning-plasma regimes in high-field, compact tokamaks *Nucl. Fusion* **62** 042003
[67] Giruzzi G *et al* 2020 Physics and operation oriented activities in preparation of the JT-60SA tokamak exploitation *Nucl. Fusion* **57** 085001
[68] Eich T *et al* 2013 Scaling of the tokamak near the scrape-off layer H-mode power width and implications for ITER *Nucl. Fusion* **53** 093031
[69] Marinoni A, Sauter O and Coda S 2021 A brief history of negative triangularity tokamak plasmas *Rev. Mod. Plasma Phys.* **5** 6
[70] Madden N A and Hastie R J 1994 Tokamak equilibrium with anisotropic pressure *Nucl. Fusion* **34** 519
[71] Graves J P 2013 Toroidal drift precession and wave–particle interaction in shaped tokamaks with finite beta and neoclassical equilibrium effects *Plasma Phys. Control. Fusion* **55** 074009